J. Fluid Mech. (1988), *vol.* 191, *pp.* 137–176
Printed in Great Britain

Structure of a turbulent boundary layer on a concave surface

By ROBERT S. BARLOW AND JAMES P. JOHNSTON†
Combustion Research Facility, Sandia National Laboratories, Livermore, CA 94550, USA

(Received 12 March 1987 and in revised form 17 October 1987)

The effects of concave curvature on turbulent boundary-layer structure are investigated, using flow visualization and two-component laser-Doppler anemometry. Destabilizing curvature amplifies large-scale motions normal to the wall. When the boundary layer entering the curve is free of spanwise non-uniformities, the resulting large-eddy structure does not consist of distinct longitudinal vortices, as suggested by some previous studies. Rather, the visualized flow is dominated by large eddies (inflows and outflows) that have a streamwise extent of only a few boundary-layer thicknesses, are quite unsteady, and do not cause significant spanwise variations in the mean properties of the boundary layer. Mixing across the boundary layer is enhanced by the new eddy structure, bringing high-momentum fluid closer to the wall than in a normal, flat boundary layer and causing a significant increase in skin friction. Spectral results show that increases in turbulence intensities and Reynolds shear stress across the outer layer are due almost entirely to increased energy in low-frequency, large-scale fluctuations.

Flow visualization suggests that the large-scale inflows and outflows have strong influence on flow structure in the near-wall region. However, when the local value of the friction velocity, u_τ, is used for scaling, near-wall profiles of Reynolds-averaged quantities show relatively minor differences between the flat and concave cases.

The response of the boundary layer to the sudden onset of concave curvature is found to involve two overlapping stages. First, a centrifugal mechanism causes higher-velocity eddies near the start of curvature to migrate toward the wall, while lower-velocity eddies migrate away from the wall. These negatively correlated motions produce an increase in the magnitude of the correlation coefficient within a few initial boundary-layer thicknesses (δ_0) from the start of curvature. The further development of the layer requires the slower growth and amplification of the large-scale inflows and outflows. This development of the new large-scale eddy structure continues for at least 20 δ_0.

1. Introduction

A concave, turbulent boundary layer is considered to be a complex turbulent flow in that the fluid is subject to an extra strain rate. In addition to simple shear, $\partial\bar{U}/\partial y$, there is a rate of strain associated with curvature of the mean streamlines which is equal to $-\bar{U}/r$, where r is the streamline radius of curvature, positive for convex and negative for concave flows. Bradshaw's (1973) review of streamline curvature made it clear that the effects of extra strain rates are large, being an order of magnitude greater than would be predicted by straightforward extensions of

† Mechanical Engineering Department, Stanford University

calculation methods for simple shear layers. The effects of concave curvature are significant even for cases in which the radius of curvature is 100 times the boundary-layer thickness (Meroney & Bradshaw 1975; Ramaprian & Shivaprasad 1978; Hoffmann, Muck & Bradshaw 1985). Furthermore, several investigators have reported large spanwise variations in boundary layers on concave surfaces that were quite persistent in the streamwise direction. For example, So & Mellor (1975) reported 100% spanwise variations in boundary-layer thickness and momentum thickness, and Meroney & Bradshaw measured a 20% variation in skin friction.

The spanwise variations are believed to be caused by large-scale roll cells that develop in the boundary layer over a concave surface. These roll cells are produced by the same type of centrifugal instability mechanism that leads to the formation of Taylor–Görtler vortices in a concave, laminar boundary layer.† However, the roll cells in the turbulent case are not nearly so well defined. While some workers have reported clear spanwise variations and attributed these to streamwise vortices, others have found no evidence of such structures in time-averaged measurements. When stable patterns were observed, the spanwise wavelength was irregular with a typical magnitude of one to two times the boundary-layer thickness.

It is this tendency toward three-dimensionality that makes the concave boundary layer fundamentally different from the convex boundary layer, which remains two-dimensional. Predictions of convex flows by mixing length models (Adams & Johnston 1983) and by k,ϵ models (Gibson, Jones & Younis 1981; Humphrey & Pourahmadi 1981) have been relatively successful. However, turbulence models have yet to predict the effects of concave curvature satisfactorily (Brown & Martin 1982), and questions have been raised as to whether turbulence models that are two-dimensional can adequately treat the concave case.

This study is a part of an ongoing research effort at Stanford to investigate the effects of curvature on turbulent boundary layers. Gillis & Johnston (1983) and Simon *et al.* (1980) reported the effects of convex curvature in terms of fluid mechanics and heat transfer, respectively. Jeans & Johnston (1982, 1983) carried out an extensive flow-visualization study in a concave boundary layer, while Simonich & Moffat (1982) investigated the heat-transfer effects in the same flow, using a liquid-crystal technique. The current study built upon the work of Jeans & Johnston and was carried out in the same facility. The overall objectives were to gain a better understanding of the concave turbulent boundary layer by obtaining detailed turbulence measurements in a flow in which the global behaviour of the large-scale roll cells was well characterized through visualization.

This paper presents results for a concave, natural boundary layer, in which the roll cells did not have stationary spanwise locations but where the layer remained nearly two-dimensional in the mean. A second case was also studied, in which vortex generators were used to create a controlled disturbance that was amplified by concave curvature to produce a stable streamwise pattern of roll cells. The local effect of these fixed structures on the bursting process is reported in Barlow & Johnston (1988). Further details regarding the vortex generator case may be found in Barlow & Johnston (1985).

† This instability mechanism was first described through inviscid arguments by Rayleigh (1917).

1.1. *Terminology, origin, and behaviour of the large-scale structures found in the concave boundary layer*

Tani (1962) was the first to measure spanwise variations of mean velocity in a concave turbulent boundary layer and to attribute these to the presence of streamwise vortices. By analogy to the laminar stability analysis of Görtler (1940), Tani argued that streamwise vortices, having a predictable range of wavelengths, should be expected in the turbulent case. Since then, the terms Taylor–Görtler vortices, longitudinal vortices, or streamwise vortices have generally been used to describe postulated structures in concave turbulent boundary layers that have produced spanwise variations in measured quantities. However, the extensive flow-visualization studies by Jeans & Johnston (1982) showed that the large-scale structures in the concave turbulent boundary layer could not be described as vortices under any reasonable definition of the term.† The structures visualized in their flow did not have well-defined cores of concentrated vorticity, had limited lifetimes, and had coherent lengths in the streamwise direction of only a few boundary-layer thicknesses. These structures were observed to wander in span, merge, separate, appear, and disappear. They seemed to be distributed randomly in space and time over the concave wall, and they did not produce significant spanwise variations in time-averaged quantities. Jeans & Johnston (1982) described these visualized large-scale structures as large-scale sweeps and ejections. Unfortunately, association of the terms 'sweeps' and 'ejections' with near-wall structures having smaller scales is likely to be a source of confusion. More appropriate terms for the large-scale structures in the concave boundary layer are large-scale inflows, large-scale outflows, and roll cells.‡

Crane & Sabzvari (1984) studied vortices in concave laminar and low-Reynolds-number turbulent boundary layers using a combination of flow visualization and laser–Doppler anemometry. Some of their visual observations regarding the unsteady behaviour of the large-scale structures in the turbulent flow are consistent with those of Jeans & Johnston and bear repeating. 'Visualization of cross-sections in the downstream half of each bend...showed accumulation of hydrogen bubbles resembling those at upwash positions in the laminar flow. These accumulations maintained roughly constant z-positions...for a few seconds, then either dispersed or merged with a neighboring accumulation.'

These visualization studies give greater credibility to previous studies, such as those by Eskinazi & Yeh (1956) and Ramaprian & Shivaprasad (1978), in which no spanwise variations were reported. They also raised the question as to whether the spanwise variations observed in some experiments might be caused by upstream non-uniformities in flow, such as those that can be produced by turbulence-damping screens.

Bradshaw (1965) determined that spanwise non-uniformities in shear stress on a flat wall could be traced to non-uniform flow through the final screen in the settling

† We consider a longitudinal vortex to be a region of fluid highly extended in the flow direction (aspect ratio greater than 10:1) with relatively high streamwise vorticity, such that fluid particles near the core perform several rotations during their stay within the vortex.

‡ Use of the term roll cell follows the work of Lezius & Johnston (1976), who studied the effects of rotation on turbulent channel flow. The effects of rotation are stronger than, but qualitatively similar to, the effects of curvature. They observed large-scale structures similar to those observed in the concave boundary layer.

chamber. In his review of the effects of curvature, Bradshaw (1973) suggests that such disturbances, depending on their strength compared to turbulent fluctuations, are likely to affect the location of roll cells either by locking them to the locations of the initial disturbances or by creating preferred locations where there is higher-than-average probability of the occurrence of a roll cell.

Swearingen & Blackwelder (1983) investigated parameters controlling the spacing of streamwise vortices in concave laminar boundary layers and concluded that the spanwise pattern of variations in velocity depended strongly on the last settling chamber screen. In reporting results of their study of concave laminar boundary layers, Crane & Sabzvari (1984) state that tests 'involving the transposition and reorientation of the screens have shown clearly that the final screen is the source of disturbances that are amplified into the Görtler vortex system.' Similar behaviour was observed in the present facility and screens had to be carefully installed and cleaned to avoid preferred locations for roll cells.

Thus there is strong evidence that spanwise non-uniformities in the upstream boundary layer have an important, if not dominant, influence on the location of roll cells in concave boundary layers. In most previous experiments, these disturbances have originated from turbulence-damping screens. However, they can come from more controllable sources. For example, Hoffmann *et al.* (1985) used an array of small vortex generators in the settling chamber of their wind tunnel to produce a fixed array of vortices in a concave turbulent boundary layer. One might expect such upstream disturbances to be amplified by concavity if they are within the range of unstable wavelengths, and the spacing of the resulting system of stationary roll cells is believed to be produced through an interaction between the upstream disturbances and the centrifugal instability mechanism. By implication, those cases in which no evidence of stationary roll cells was found must have been relatively free of upstream non-uniformities in the mean flow. In these cases, the formation of transitory roll cells was probably brought about through the amplification of the existing, randomly distributed, large-scale eddies at the start of curvature. Work of Kovasznay, Kibens & Blackwelder (1970), Falco (1977, 1978) and Brown & Thomas (1977) indicates that large-scale eddies in a flat boundary layer are roughly δ in width. This width is consistent with the typical spanwise wavelength of transitory roll cells observed by Jeans & Johnston and in the present study.

In general one should expect large structures in concave boundary layers to exhibit a range of behaviours from essentially steady vortices, when upstream non-uniformities are large and of appropriate wavelength, to short randomly distributed roll cells, when the upstream boundary layer is uniform in the mean.

Some useful insights regarding the interaction between upstream disturbances and the instability mechanism can be obtained by applying Tani's approximate approach to some of the more recent data on the spanwise wavelength of observed roll cells or measured variations in concave turbulent boundary layers. The Görtler number is normally defined as $Gr = Re_\theta(\theta/r)^{\frac{1}{2}}$ for laminar flows, where θ is the momentum thickness and r is the radius of curvature. By substituting the eddy viscosity for the kinematic viscosity in Re_θ and by making some assumptions about the shape parameters of the boundary layer, Tani arrived at the approximate turbulent form, $Gr_T = 43(\theta/r)^{\frac{1}{2}}$. This form was used to locate data for the wavelength of spanwise variations from several experiments on the stability curves in figure 1 calculated for a laminar boundary layer by Ragab (1979). The data for relatively strong curvature (i.e. So & Mellor 1975, 1978; Shizawa & Honami 1985; Jeans & Johnston 1982, 1983 and the present experiment) lie well inside the unstable region and close to the line

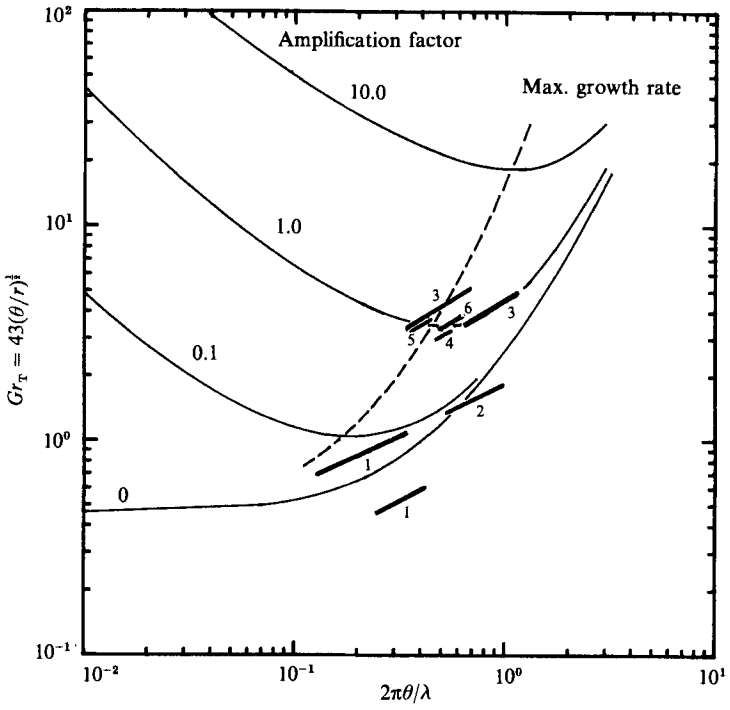

FIGURE 1. Approximate turbulent Görtler stability parameter *vs.* roll-cell wavelengths in concave boundary layers from 1, Tani; 2, Muck; 3, So & Mellor; 4, Shizawa & Honami; 5, Jeans & Johnston; 6, Barlow & Johnston (1985).

of maximum growth rate. Interestingly, some of Tani's data lie below the neutral stability curve. The data of Muck (1982) barely intersect the unstable region, even though the vortex generators that determined the wavelength, λ, for the latter case were chosen to maximize the amplification of the spanwise variation of C_f. The stability analysis is based on small perturbations of a laminar velocity field, but the disturbances in a turbulent boundary layer, whether from fixed sources or from the turbulence motions, are hardly small perturbations. Thus, it is not surprising that roll cells can develop in turbulent flows at equivalent Görtler numbers for which laminar flows would be stable. Furthermore, the lines of constant amplification factors have very broad minima, indicating that the centrifugal instability mechanism can amplify a wide range of wavelengths. The 1:2 slope of the data sets in figure 1 shows that the observed wavelength did not change significantly as the boundary layer grew in any of the included experiments. The spanwise wavelength must eventually increase as the boundary layer thickens. However, the bandwidth of unstable wavelengths appears to be broad enough to allow the initial wavelength to persist through a doubling of the boundary-layer thickness.

1.2. *Previous measurements on turbulence structure in concave flows*

Several previous investigations have provided relatively detailed data on turbulence structure in concave boundary layers, particularly on the Reynolds stresses; such data are essential for the evaluation of prediction methods and the development of improved models.

So & Mellor (1972, 1975, 1978) studied a case of strong curvature ($0.1 < \delta/R < 0.2$),

and used hot-wire anemometry to obtain profiles of all six Reynolds stresses at locations corresponding to maxima and minima in their spanwise surveys of mean velocity. They found only a very limited region of near-wall similarity, extending no farther from the wall than $y^+ = 50$. (The following definitions are used throughout this paper: $y^+ = yu_\tau/\nu$, where y is distance normal to the wall, u_τ is the local friction velocity, and ν is the kinematic viscosity; $u^+ = \bar{U}/u_\tau$, where $\bar{U}$ is the mean streamwise velocity. Angle brackets, $\langle\ \rangle$, indicate the time average of a given turbulence quantity, and a prime indicates an r.m.s. value, i.e. $u' = \overline{\langle u^2 \rangle}^{\frac{1}{2}}$ is the r.m.s. streamwise turbulence intensity.) Another notable result was the existence of secondary peaks in the profiles of $\langle u^2 \rangle$, $-\langle uv \rangle$, and the correlation coefficient, R_{uv}, near $y/\delta = 0.8$ at their station 4, which corresponded to a mean outflow or 'upwash' region. These results indicated an unusually high degree of turbulence activity in the outer part of the boundary layer.

Ramaprian & Shivaprasad (1978) conducted experiments on the effects of mild concave and convex curvature and reported a variety of data on turbulence structure. They concluded that the rate of turbulence production was not significantly increased by concave curvature but that turbulent diffusion, as determined from triple products, was strongly affected.

Hunt & Joubert (1979) considered developing flow in a mildly curved duct. Based on comparisons with previous studies of strong curvature, they advocated that a distinction be made between 'shear dominated' flows and 'inertia dominated' flows, the latter tending to develop significant regions of constant or near-constant angular momentum (Ur) in the mean-flow profiles. By comparing streamwise velocity spectra for flat, convex, and concave flows, they determined that differences in streamwise turbulence intensity were associated with changes in the energy content in the low-wave-number range alone. In §3.6, we shall see that the same is true of spectra of velocity fluctuations normal to the wall and of the Reynolds shear stress, $-\langle uv \rangle$.

Prabhu & Rao (1981, 1982) reported turbulence data for concave boundary layers having three values of the curvature parameter ($\delta_0/R = 0.024$, 0.054, 0.078). Their wind tunnel had a low aspect ratio, but an effort was made to minimize the effects of secondary flow from the endwalls. All Reynolds stresses but no triple products were measured along the channel centreline between a peak and valley in the spanwise pattern of mean velocity. The amplitude of the spanwise pattern decreased through the curve, so that the behaviour of roll cells was unclear.

Muck (1982) provided a comprehensive data set on the effects of mild concave and convex curvature on turbulent boundary layers (see also Muck, Hoffmann & Bradshaw 1985; Hoffmann *et al.* 1985). He used the same flow facility as Meroney & Bradshaw (1975), but, following Hoffmann & Bradshaw (1981), he installed an array of small vortex generators in the settling chamber to control the spanwise distribution of stationary roll cells in the boundary layer on the concave wall. Hot-wire measurements were made at two spanwise locations corresponding to maximum C_f (inflow) and minimum C_f (outflow) for each of five streamwise stations. He concluded that the effects of convex and concave curvature were 'totally different', and that the response of the boundary layer to a step increase in concave curvature was an order of magnitude slower than that for convex curvature. Significant differences in turbulence structure between the two spanwise locations were found, even in this case of mild curvature.

A different conclusion regarding the response of a boundary layer to concave curvature was reached by Shizawa & Honami (1983, 1985). They studied a case of moderate curvature ($\delta_0/R = 0.046$), looking specifically at the region near the start

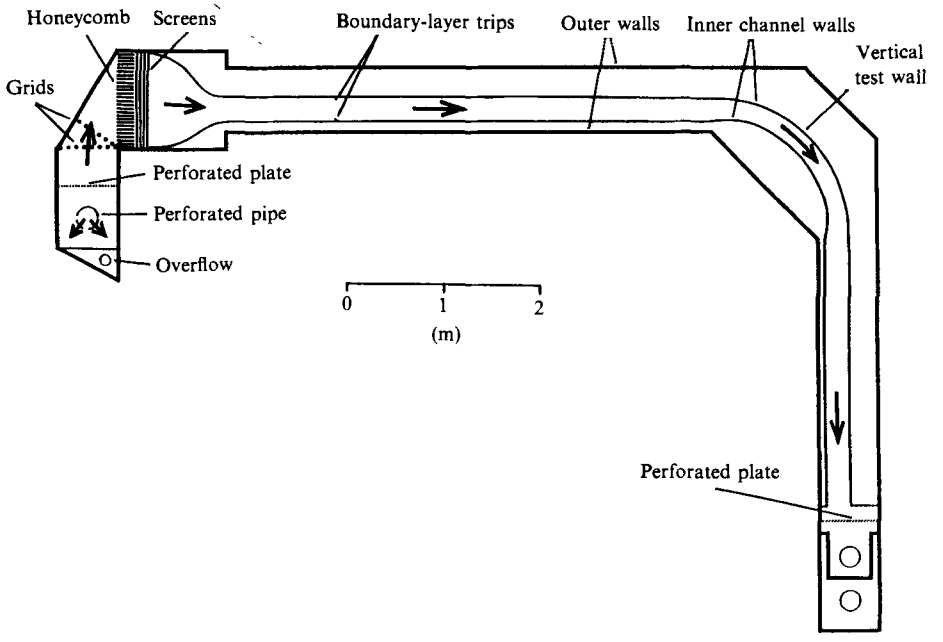

FIGURE 2. Schematic of the flow facility.

of the curve. They concluded that the mean flow and the Reynolds stresses responded 'rapidly' to rapid increase (from zero) of the effective curvature. Further discussion of their results is included in §3.4.

The present paper documents an extensive flow visualization and LDA survey of a concave, natural boundary layer. The flow facility, visualization techniques, and the LDA system are described in §2, along with a discussion of the accuracy of the near-wall data. Section 3 presents and discusses visualization results, profiles of Reynolds-averaged turbulence quantities, and turbulence spectra. These data clarify the nature of the large-eddy structure that develops in the concave boundary layer, the mechanism of response of a turbulent layer to the sudden onset of wall curvature, and the effects of curvature on the near-wall region.

2. Experimental apparatus and techniques

2.1. *Flow facility*

Experiments were performed in a large, low-speed, free-surface water channel that was designed and built for the previous studies by Jeans & Johnston and Simonich & Moffat. The schematic in figure 2 shows two sets of walls: the outer, load-bearing walls that are held by steel frames, and the inner, movable walls that define the flow channel. Note that the test wall is vertical. Water is pumped from an underground sump and enters the inlet section through a perforated pipe. Flow conditioning is provided by a perforated plate, two large-open-area grids, a four-inch section of $\frac{1}{4}$-inch-cell honeycomb, four screens, and an asymmetric 4:1 contraction. The water flows down a 488 cm-long, straight development section at a nominal velocity of 15 cm/s. Boundary layers on both walls are tripped about 100 cm downstream of the contraction. Parameters of the boundary layer at the flat station ($x = -88$ cm, $z = 0$)

	Station			
	Flat	15°	30°	60°
x (cm)	−88	35	71	142
z (cm)	0.0	−5.0	−5.0	−5.0
U_{pw} (cm/s)	14.9	13.4	14.8	14.8
u_τ (cm/s)	0.683	0.646	0.732	0.773
ν (cm^2/s)	0.0099	0.0103	0.0102	0.0104
δ_{99} (cm)	6.35	7.67	9.01	12.05
δ_{99}/R	0.000	0.056	0.066	0.088
δ^* (cm)	1.10	1.28	1.38	1.45
θ (cm)	0.76	0.94	1.05	1.18
Re_θ	1140	1220	1540	1680
H	1.46	1.37	1.31	1.23
G	6.87	5.66	4.83	3.58
C_f (log law)	0.0042	0.0046	0.0049	0.0054

x, z, System coordinates. See figure 3: U_{pw}, Potential velocity extrapolated to the wall; u_τ, Friction velocity; δ^*, Displacement thickness defined in §3.2; θ, Momentum thickness defined in §3.2; Re_θ, Momentum thickness Reynolds number, $U_{pw}\theta/\nu$; H, Shape factor, δ^*/θ; G, Clauser shape factor, $(2/C_f)^{\frac{1}{2}}(H-1)/H$; C_f, Skin-friction coefficient.

TABLE 1. Parameters for two-component profiles

before the start of wall curvature are listed in table 1 and are in good agreement with data for zero-pressure-gradient boundary layers at similar Reynolds numbers, as reviewed by Smits *et al.* (1983). At the beginning of the curved section ($x = 0$) the boundary layer on the test wall is about 7.5 cm thick and has a momentum thickness Reynolds number of about 1300. The free-stream turbulence level at this location is about 0.7% of free-stream velocity. This boundary layer is subjected to a 90° concave curve of constant radius ($R = 136$ cm), followed by a recovery section. Figure 3 shows the dimensions of the concave test wall and the coordinate system used in describing the data.

The wall opposite the test wall is contoured to minimize pressure gradients on the test wall, so the channel width varies somewhat about its nominal value of 25 cm. The contour design is based on potential flow analysis and accounts for boundary-layer displacement thicknesses (Jeans & Johnston 1982). Pressure gradient could not be measured to useful accuracy, owing to the low velocities in the channel and the presence of the free surface. However, the streamwise variation of U_{pw}, the extrapolation to the wall of the potential velocity determined by fitting the velocity profile in the free stream, is less than 3% at the nominal operating condition of the channel. The low value in table 1 for U_{pw} at the 15° station is due to operation of the channel at a flow rate slightly below normal for this run. This low value is not the result of streamwise pressure gradients.

The aspect ratio based on the boundary-layer thickness at the start of curvature is 14:1. Jeans & Johnston determined that pressure-driven secondary flows near the bottom wall do not affect the centre region of the vertical test wall, where

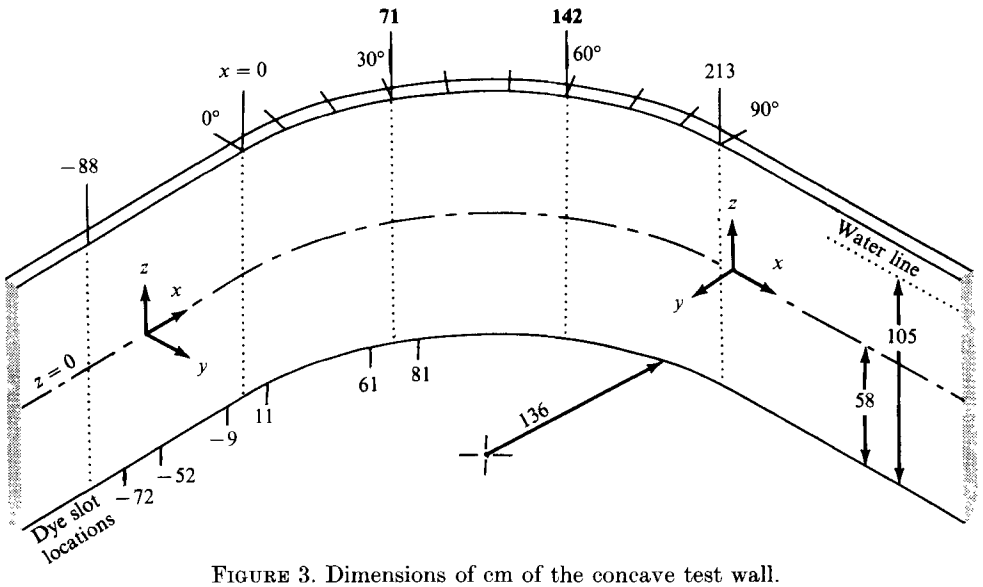

FIGURE 3. Dimensions of cm of the concave test wall.

measurements are made. They also determined that the boundary layers on the two walls began to merge about 75° into the curve. Accordingly, the current study focuses on the turbulence structure of the flow at 60° of turn, approximately 20 initial boundary-layer thicknesses from the start of curvature. Data included in this paper suggest that major structural changes have occurred by this streamwise station.

2.2. *Flow-visualization methods*

Two flow-visualization techniques were used in this study: conventional coloured-dye visualization and laser-induced-fluorescence (LIF) flow visualization. In both techniques, dye was injected at very low speed into the sublayer through narrow slots spanning the middle portion of the test wall (-15 cm $< z <$ 15 cm). Locations of the dye slots are shown in figure 3.

For LIF flow visualization a sheet of argon-ion laser light was directed downward into the water channel to illuminate a spanwise plane perpendicular to the test wall. Fluorescene sodium salt, diluted in water to 0.5 g/l, was injected through a dye slot upstream of the laser sheet. The dye collected into the low-speed streaks, then mixed out into the boundary layer and fluoresced as it passed through the laser sheet, marking fluid that originated at the wall. The laser sheet was positioned at two streamwise locations: on the flat wall at $x = -12$ cm and on the curved wall at 60° of turn, with dye being injected 60 cm (several boundary-layer thicknesses) upstream of each position.

2.3. *Laser-Doppler anemometry system*

All velocity data were obtained using a TSI two-colour, three-beam, laser-Doppler anemometry system. This system included a 2 W argon-ion laser, a single Bragg cell, a 3.75:1 beam expander, and two TSI 1980A counters. Laser beams were directed downward into the channel through a window placed at the water level.

Some measurements of streamwise velocity were obtained using the back-scatter configuration. However, that configuration proved inadequate for two-component

measurements. With backscatter, the measured values of the Reynolds shear stress, $-\langle uv \rangle$, in the flat boundary layer were clearly too low inside of about $y/\delta = 0.2$, even though the profiles of u' and v', the streamwise and normal turbulence intensities, were in good agreement with those of Eckelmann (1974) well into the viscous sublayer. The low uv correlation was caused by the presence of multiple particles in the measuring volume. With multiple particles, Doppler signals on the two channels may be validated at essentially the same time but may not be from the same particle. The measuring volume in backscatter was cigar-shaped, being only 0.2 mm in diameter but nearly 7 mm long. This corresponded to a non-dimensional spanwise length ($z^+ = zu_\tau/\nu$) of about 50 viscous units in the present flow. The two-point spanwise correlation coefficient for u fluctuations drops off very rapidly with z^+ distance near the wall (Gupta, Laufer & Kaplan 1971), due to the structure of the sublayer streaks. Thus it is essential to have a small measuring volume to obtain accurate cross-correlations in a highly seeded flow. Hot-wire studies on near-wall structure (Blackwelder & Haritonidis 1983; Willmarth & Sharma 1984) have concluded that wire lengths of 20 viscous units or less should be used near the wall if 'eddy-averaging' effects are to be avoided.

A 90° side-scatter configuration, with receiving optics mounted to the side of the flow facility, was used for all two-component measurements. This arrangement provided an effective measuring volume that was approximately 0.2 mm in diameter ($\Delta y^+ \approx 1.5$) and 0.4 mm in length ($\Delta z^+ \approx 3$), whereas the Kolmogorov scale was determined to be about 2 viscous units.† The beams were oriented in the 0/90 configuration with the blue channel measuring streamwise velocity, U, and the green channel measuring the normal velocity, V. Shift frequencies of 50 kHz on each channel provided effective fringe velocities that were roughly twice the free-stream velocity.

The signal quality (signal-to-noise ratio) obtained in side scatter was superior to that in backscatter, due primarily to the elimination of stray reflected light. However, the signal amplitudes were weak, and two Keithley Instruments 102BR-L isolation amplifiers were used to boost the signals going into the counters by a gain of 10. The TSI 1980A processors were set to count 16 fringes using a 1% comparison check. Signals from the TSI 1988 analog output units were sampled at uniform intervals. LDA data rates were typically at least an order of magnitude higher than the A/D sampling frequency and were considerably higher than any significant energy-containing frequencies in the flow. Data for Reynolds-averaged results were acquired by a Digital Equipment Corporation MINC computer, and turbulence statistics included here are based on 12000–15000 samples taken over 10–12.5 minute periods. The large sample size was required to obtain stationary values for the skewness of v. Data for spectral analysis were acquired by a VAX 11-750 computer and were stored on digital tape for subsequent processing.

2.4. *Accuracy of the near-wall measurements*

Near-wall measurements are inevitably constrained by physical limitations. Therefore, it is essential to establish the range of accuracy of any near-wall data set. Mean streamwise velocities, $\bar{U}$, could be measured as close to the wall as $y^+ = 1.5$. However, since these near-wall mean data were extrapolated to $y = 0$ to establish the location of the wall, we can make no new contributions regarding the shape of the

† The estimate of the Kolmogorov scale is based on measured values of $\partial\bar{U}/\partial y$ and $-\langle uv \rangle$ at $y^* = 15$ and on the assumption that dissipation is equal to production at that location.

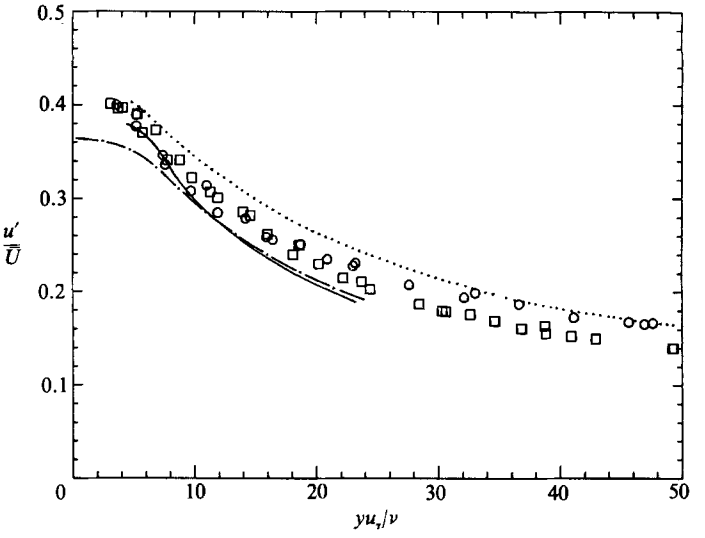

FIGURE 4. Comparison of profiles of $u'/\bar{U}$ in the near-wall region: □, flat station; ○, 60° station; ——, Kreplin & Eckelmann (1979); –·–, Kim *et al.* (1986); · · · · ·, Klebanoff (1954).

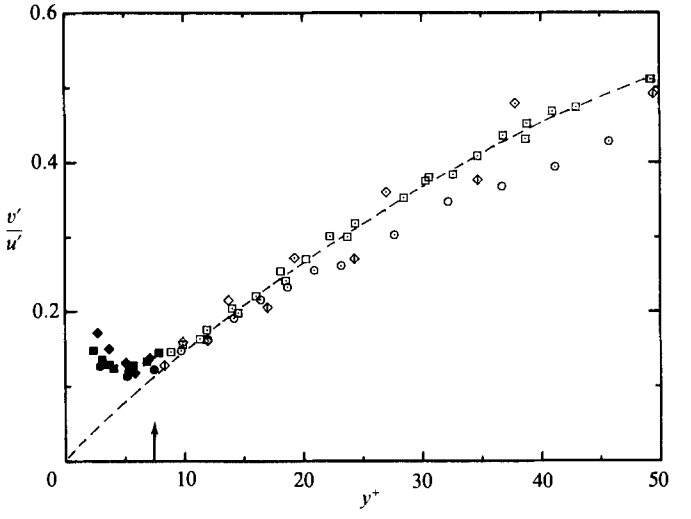

FIGURE 5. Profiles of v'/u' in the near-wall region show that reduced signal-to-noise ratio for the v signal produces errors in v' from about $y^+ = 7$ inward. □, flat; ◇, 15°; ◈, 30°; ○, 60°; ---, expected trend.

mean-velocity profile within the sublayer. This is not considered to be a limitation with regard to interpretation of the turbulence data, since the uncertainty in wall location resulting from the extrapolation procedure was small (± 0.03 mm or ± 0.2 wall units for data sets with at least two points inside $y^+ = 5$.

Close to the wall, the velocity gradient, $\partial \bar{U}/\partial y$, becomes large relative to the y-dimension of the measuring volume. While this does not significantly affect measurement of the mean velocity by the technique used here, it causes a broadening of the signal that results in a bias in the measured values of u', the r.m.s. streamwise turbulence intensity (Karpuk & Tiederman 1976). An approximate analysis given by Barlow & Johnston (1985) indicates that the u' data are about 10% high at $y^+ = 4$,

due to this gradient broadening. Figure 4 shows profiles of $u'/\bar{U}$ and provides a comparison of present measurements with experimental and computational results from the literature. This comparison suggests that a 10% u' bias at $y^+ = 4$ is a reasonable if not generous estimate. Since this bias effect decreases rapidly with distance from the wall, no correction for this u' error has been applied to the data presented here.

Limitations on measurement of v', the r.m.s. intensity of velocity fluctuations normal to the wall, can be assessed from figure 5, which shows the behaviour of v'/u' close to the wall. From considerations of continuity, this ratio should be linear in y in the limit as y goes to zero. Figure 5 shows that the v' data begin to deviate from the expected trend inside $y^+ = 10$, because the signal-to-noise ratio decreases as v' becomes very small. The error in v' may exceed 10% by y^+ of 7 or 8, so that v' and the uv cross correlations could not be measured accurately within the sublayer. Except for results in figure 5, none of the data including v measurements is presented for y^+ below 7.

3. Results and discussion

3.1. *Flow visualization*

Striking differences in the structures of the flat and concave boundary layers were revealed by both visualization techniques. In the flat boundary layer, the coloured-dye technique (figure 6*a*, plate 1) shows the well-known streaky structure of the sublayer, which was first documented by Kline & Runstadler (1959). These streaks had a typical spacing of 1.2–1.5 cm (80–100 viscous units) and appeared to be distributed uniformly across the span. The bursting events, in which dye-marked, low-speed streaks lifted up, oscillated, and broke up, distributing dye outward into the boundary layer, also appeared to be uniformly distributed. LIF photographs in the flat boundary layer support this assessment. Figure 7 includes LIF photographs with three different exposure times. The $\frac{1}{125}$ s exposure freezes the eddies. The 2 s exposure provides a short-time average view of the flow, and the 60 s exposure gives a relatively long-time average. Ejections of dye-marked fluid shown in the $\frac{1}{125}$ s exposure appear to be uniformly distributed in space and time so that the longer exposures show relatively uniform images.

A very different situation was found in the concave boundary layer. Here, the flow was dominated by intermittent, large-scale inflows and outflows, as described by Jeans & Johnston. Figure 6(*b*) (plate 1) suggests that these large-scale motions have strong effects on the near-wall region, as well as on the layer. The sublayer streaks fan out under inflow regions, while they come together under outflow regions. Inflows accelerate the sublayer, thinning it locally and spreading sublayer fluid laterally toward the outflows. LIF pictures in figure 8 reveal that the ejections of the dye are no longer uniformly distributed, as in the flat boundary layer, but are collected into the large-scale outflows. These outflows are separated by regions of fluid that are essentially clear of dye, suggesting that the bursting process, by which dye is ejected out of the sublayer, is suppressed by the large-scale inflows.

Consistent with the observations of Jeans & Johnston, the present visualization studies showed that the transitory roll cells in the concave boundary layer for the natural flow case (i.e. the flow without vortex generators) did not have stationary spanwise locations. Rather, they were observed to wander, merge, separate, appear, and disappear and seemed to be randomly distributed in space and time. The dye-marked structures occupied a range of scales but typically extended across the full

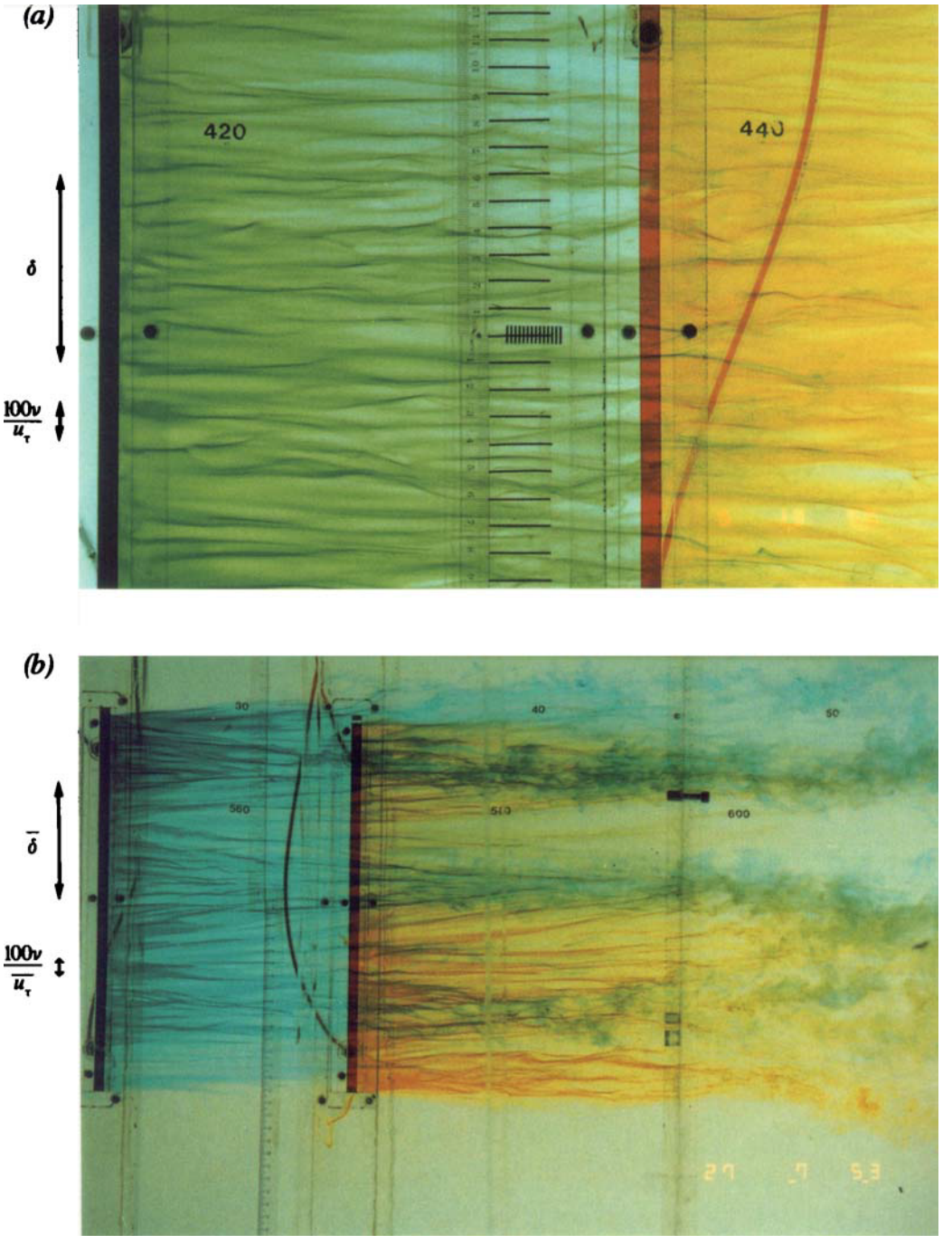

FIGURE 6. Flow visualization in *(a)* flat and *(b)* concave boundary layers.

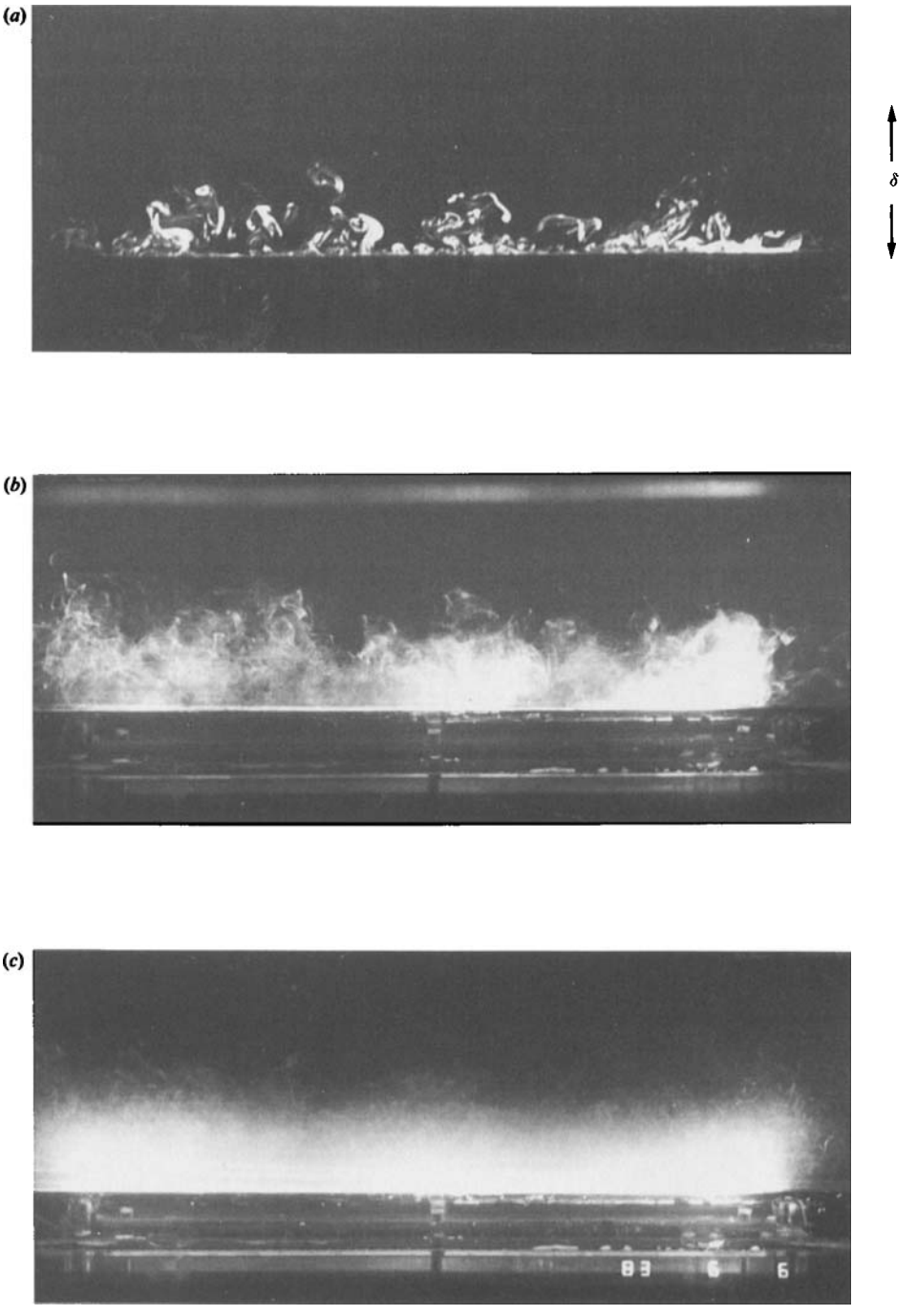

FIGURE 7. Laser-induced fluorescence photographs showing the (y, z)-plane in the natural flow, flat boundary layer with dye injected 60 cm upstream: (*a*) $\frac{1}{125}$ s exposure; (*b*) 2 s exposure; (*c*) 60 s exposure.

FIGURE 8. Laser-induced fluorescence photographs at 60° (x = 142 cm) in the natural flow showing accumulations of dye of large-scale outflow regions. $\frac{1}{125}$ s exposures.

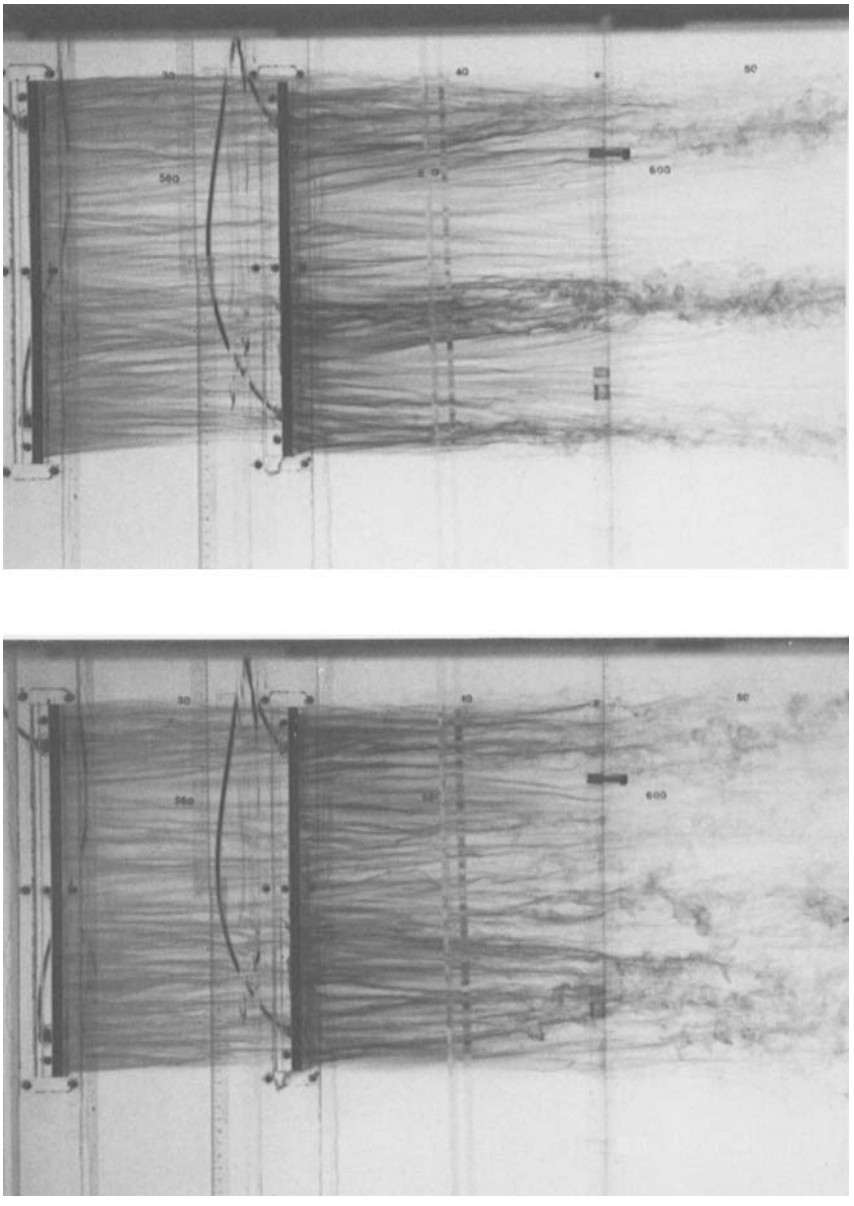

FIGURE 9. Dye-visualization photographs showing variability of the strength of transitory roll cells in the natural flow.

height of the boundary layer and were 0.5–1.0δ in span. The coherent streamwise length of the transitory roll cells was typically three to five boundary-layer thicknesses, and these structures were clearly not continuous through the entire curve, as the inappropriate term 'vortices' might imply. Coherence in the y-direction was greater than in flat boundary layers, because the centrifugal instability mechanism amplifies the intensity of large-scale motions normal to the wall. The typical streamwise length of the dye-marked structures was also somewhat greater

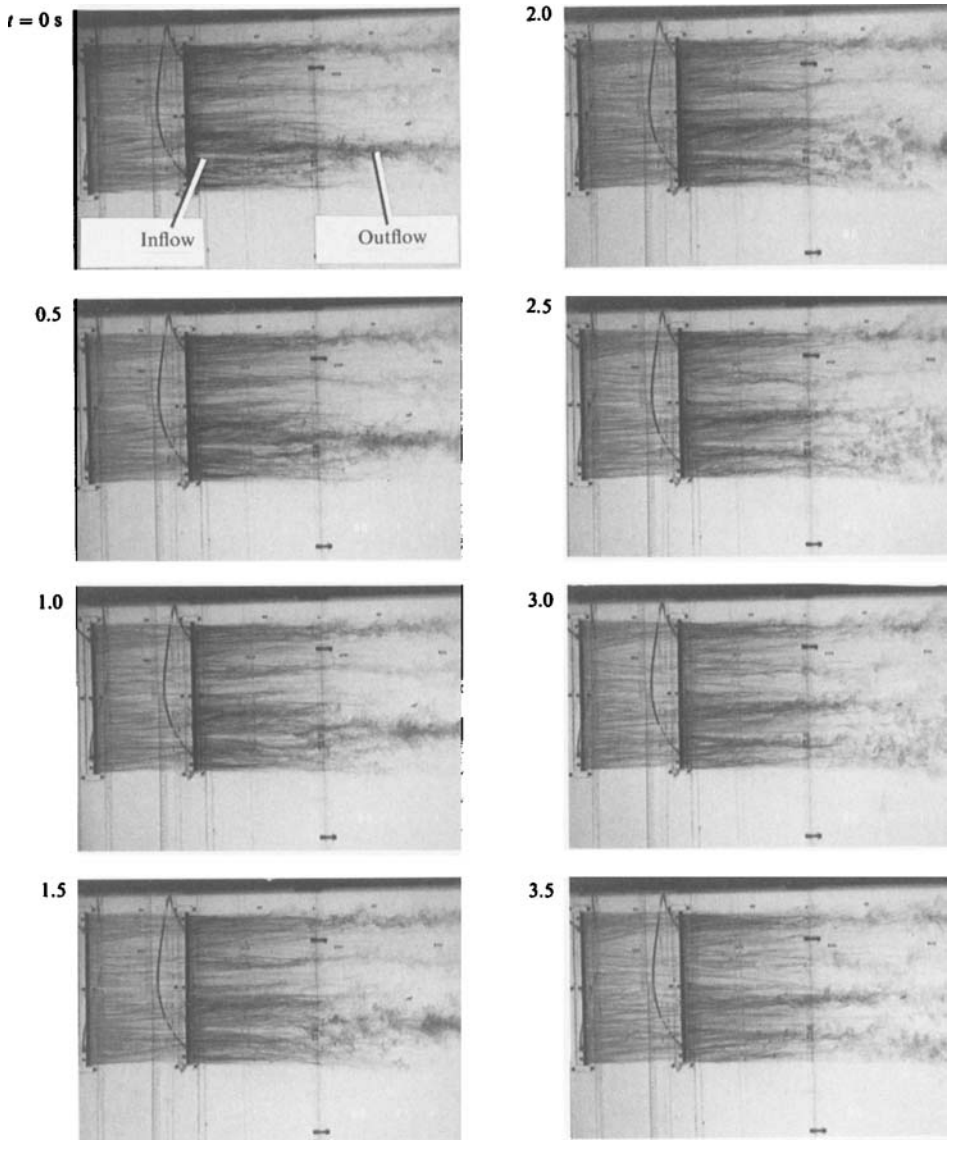

FIGURE 10. Sequence of photographs showing temporal and spatial development of a large-scale inflow following directly behind a large-scale outflow. Inflows are marked by a divergent streak pattern. Outflows are marked by a convergent streak pattern and dark concentrations of dye. The total free-stream convection distance is about 55 cm, three-quarters of the field of view.

than the length of coherent large-scale eddies in a normal flat boundary layer. (Kovasznay *et al.* (1970), Falco (1977), and Brown & Thomas (1977) reported evidence that typical large-scale coherent eddies in the flat boundary layer were roughly 2.5 to 3δ long in the streamwise direction.)

The strength of the visualized motions in the natural, concave boundary layer was quite variable. Usually, very distinct inflow and outflow regions were visible, but at times the structures were less strong and could not be easily distinguished in the coloured-dye patterns. Figure 9 includes two photographs that are representative of this variation in the strength of the transitory roll cells.

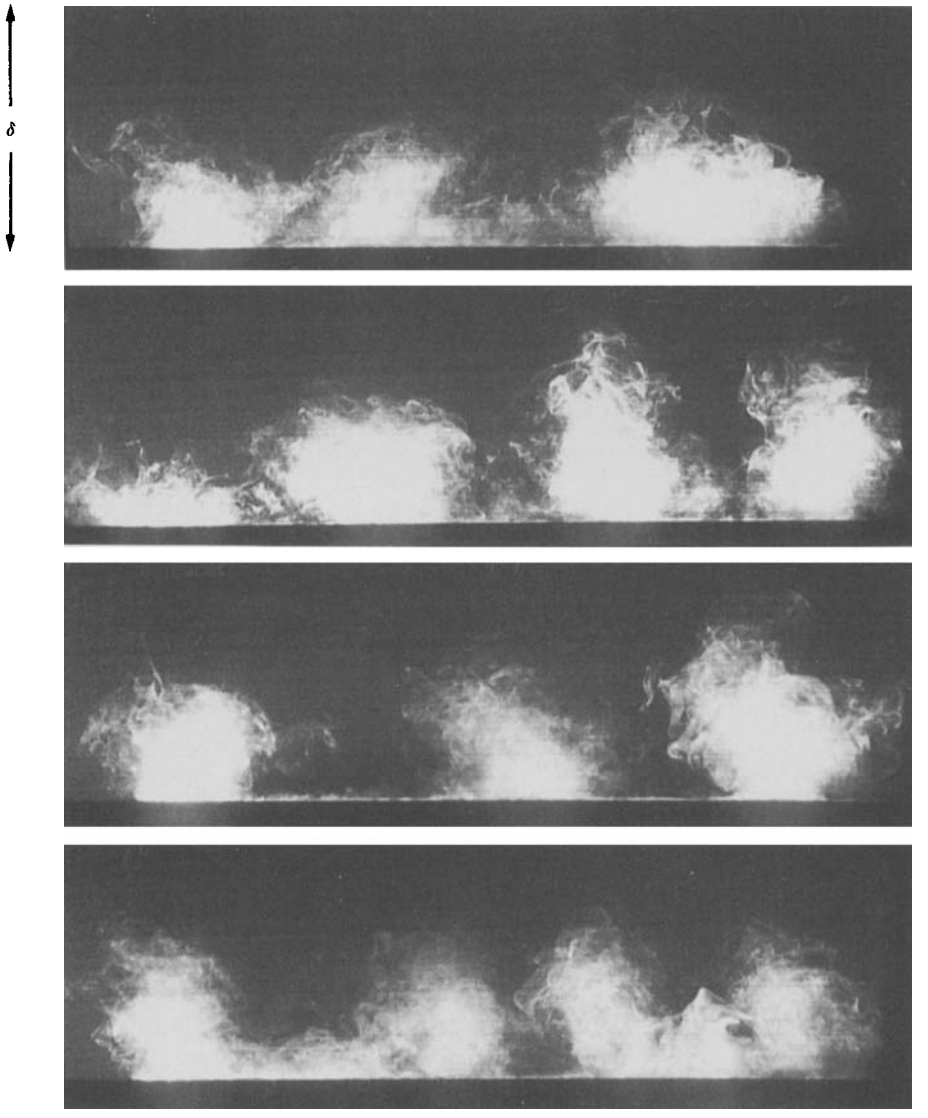

FIGURE 11. 2 s LIF exposures at 60° in the natural flow, showing distinct outflow regions that seem to appear randomly in space and time.

Figure 10 shows a sequence of coloured-dye pictures taken at half-second intervals. These give a sense of the global behaviour and temporal development of the roll cells. The field of view extends from roughly 25° to 50° of turn. In the first picture, a relatively strong outflow is located in the lower portion of the span. As time progresses and the outflow region moves downstream, the streak lines at the upstream end of the outflow structure begin to diverge, and a large-scale inflow region appears. This inflow follows directly behind the outflow and can be thought of as splitting the outflow apart or terminating the original outflow while creating two new outflows that appear on either side. This is clearly not an example of the spanwise wandering of a longitudinal roll cell that is coherent through the entire length of the curve.

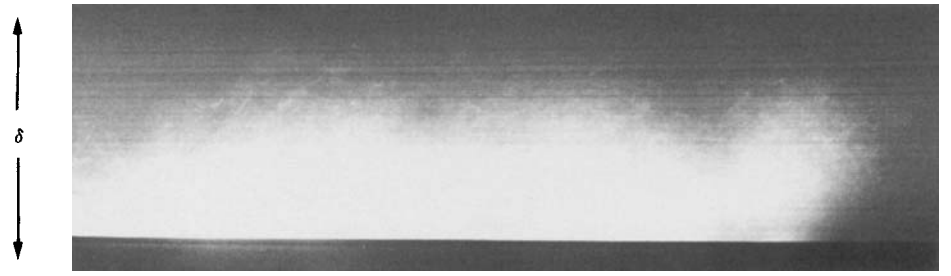

FIGURE 12. 60 s LIF exposure at 60° in the natural flow, showing a relatively uniform distribution of dye.

Another view of the behaviour of the transitory roll cells in the natural flow was provided by time exposures with the LIF technique. Several 2 s exposures taken at random intervals at the 60° location are included in figure 11. The number of outflow regions, as well as their sizes and spanwise positions, varied from frame to frame. This unsteady behaviour resulted in a relatively uniform image in a 60-second exposure shown in figure 12.

3.2. *Mean velocity profiles*

The large-scale mixing induced by destabilizing curvature brings high-momentum fluid closer to the wall, causing a steeper velocity gradient near the wall than in a corresponding flat boundary layer. As shown in figure 13, the mean velocity profiles become fuller as the boundary layer develops along the concave surface. When the velocity profiles are scaled on local wall variables (figure 14), one finds that the boundary layer can be considered in two parts. There is an inner region where profiles collapse very well according to the universal u_τ scaling, and there is an outer region where major changes are evident. The inner region extends only as far as $y^+ \cong 50$ for the present case of strong curvature and relatively low Reynolds number. So & Mellor found a similar, limited region of near-wall similarity in the mean velocity profiles for their case of strong curvature, but more extended log regions have generally been found in flows with mild curvature and in flows at higher Reynolds numbers. This behaviour is not unexpected, since the ratio of the extra strain rate to the mean shear is largest across the outer layer. However, it is still interesting that the mean-velocity profiles near the wall show no indication of the changes in visualized near-wall structure discussed above.

Outside the region of near-wall similarity, concave curvature causes the development of a negative wake function. That is, the mean velocity profile drops below the log law and remains below it out to the free stream. There appears to be a delay in the response of the mean velocity profiles to the onset of curvature, in that the change in profile shape between the 15° and 30° stations is much greater than that between the flat and 15° stations. The response rate of the boundary layer will be discussed further in §3.4.

Data on the streamwise development of the integral thicknesses, δ_{99}, δ^*, and θ, and of the shape parameters H and G, for the natural flow case are summarized in table 1. Data in the curved region of the flow are based on two-component profiles obtained at $z = -5$ cm. V-component measurements at 60°, as well as visual observations, showed this to be a location having nearly equal probability of inflows and outflows. Furthermore, C_f values for $z = -5$ cm at the 30° and 60° stations are

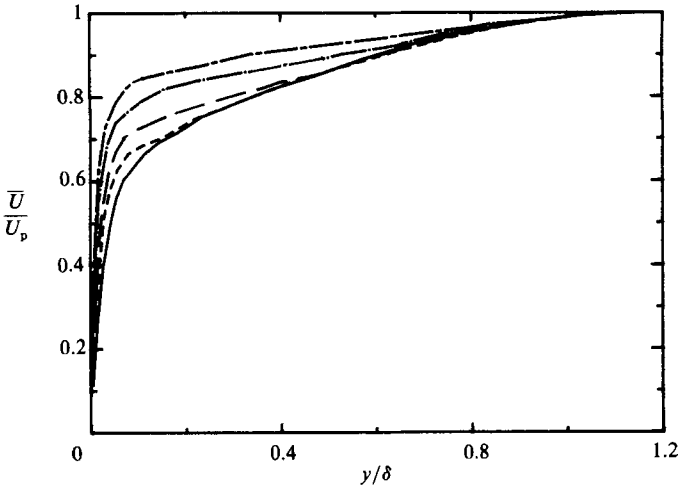

FIGURE 13. Streamwise development of mean velocity profiles in the natural flow. $\bar{U}/U_p$ *vs.* y/δ_{99}: ——, flat; – – –, 15°; ——, 30°; —·—, 60°; — — —, 75°.

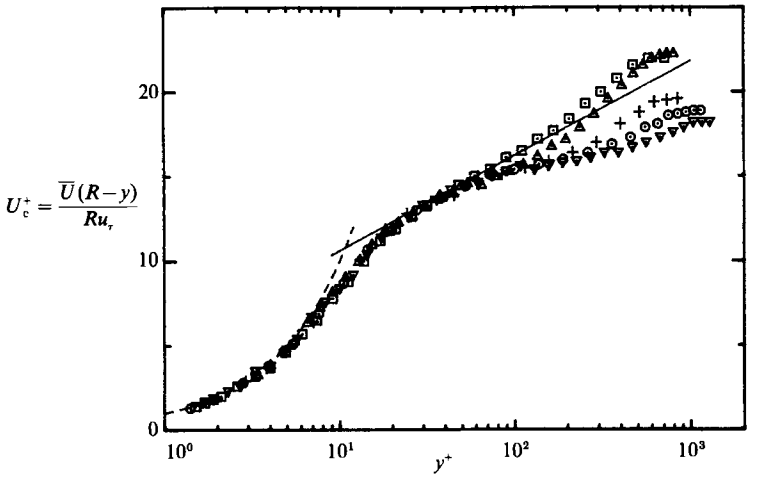

FIGURE 14. Streamwise development of mean-velocity profiles in the natural flow. $\bar{U}(R-y)/Ru_\tau$ *vs.* yu_τ/ν: □, flat; △, 15°; +, 30°; ○, 60°; ▽, 75°; ——, $u^+ = 2.44$ ln y^+ 5.0.

within 2% of spanwise average C_f values (covering the spanwise range -16 cm $\leqslant z \leqslant 16$ cm) at the same streamwise locations. Consequently, flow conditions at $z = -5$ cm are considered to be representative of a concave flow that is two-dimensional in the mean.

The integral parameters δ^* and θ for the concave boundary layers were calculated according to the formulations of Honami & Johnston (1980):

$$\delta^* = R \exp\left[\frac{1}{U_{pw} R}\int_0^\delta (\bar{U}_p - \bar{U})\,dy - 1\right],$$

$$\theta = R\left[\left\{1 - \frac{1}{U_{pw}^2 R}\int_0^\delta \bar{U}(\bar{U}_p - \bar{U})\,dy\right\}^{-1} - 1\right].$$

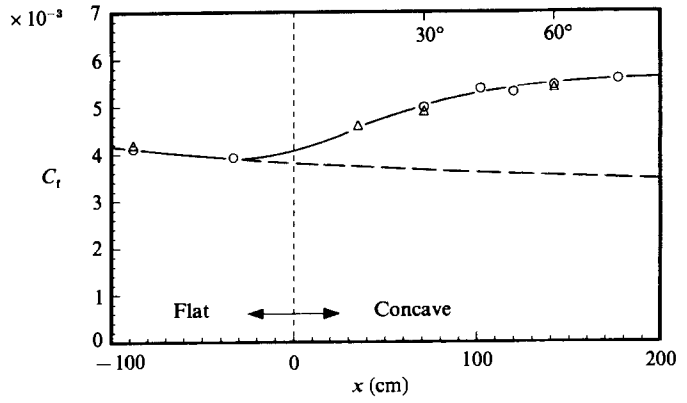

FIGURE 15. Streamwise development of ○, spanwise average C_f in the natural flow; and △, point values of C_f from table 1. The dashed line represents the expected development in a flat boundary layer.

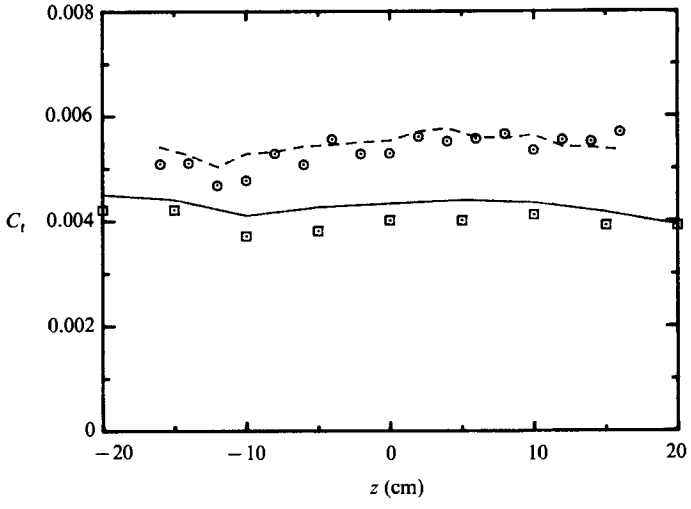

FIGURE 16. Comparison of C_f results from the Clauser method and the near-wall-slope method: ——, flat station, Clauser method; □, flat station, gradient method; – – –, 60° station, Clauser method; ○, 60°, gradient method.

Observed trends in these integral parameters are consistent with expected effects of destabilizing curvature. δ_{99} grows much more rapidly over the concave wall than over the flat wall and nearly doubles between the flat and 60° stations. However, the growth in displacement thickness is less rapid, due to the development of the fuller profile. The shape factors, H and G, both decrease substantially in the curve, also showing the effect of the development of fuller velocity profiles as the flow progresses downstream.

The streamwise development of the skin-friction coefficient, C_f, is shown in figure 15. Note that spanwise average values of C_f are included, as well as the values from table 1 for individual profiles. By the 60° station, roughly $20\delta_0$ into the curve, C_f is about 40% greater than would be expected in a flat boundary layer at the same

momentum-thickness Reynolds number. Skin friction continues to increase slightly after the 60° station, indicating that, although major changes in C_f were completed within a streamwise distance of $20\delta_0$, the boundary layer has yet to reach an equilibrium state.

The C_f data are based on local values of u_τ determined by a log–law fit using coefficients of 0.41 and 5.0. To assess the validity of the Clauser method for these profiles, wall shear was calculated from the velocity gradient close to the wall, determind from a linear least-squares fit to data points between $y^+ = 1$ and 5. The mean-velocity profile in this region deviates slightly from the simple linear law, $u^+ = y^+$. Consequently, the values of C_f obtained by the near-wall gradient method are expected to be 5–8% below the true values. Figure 16 compares C_f results from the two methods in the natural flow at the flat and 60° stations. Within the scatter of the second method, the expected relationship is found, giving reasonable assurance that the Clauser method is valid for the natural flow.

Note that there are some spanwise variations of C_f in the flat boundary layer, due presumably to disturbances from the screens upstream of the contraction. These disturbances are amplified in the curve, such that regions of lower C_f correspond to slightly preferred locations for outflows, while regions of higher C_f correspond to slightly preferred locations for inflows.

3.3. *Streamwise development of outer-layer turbulence structure*

Streamwise development of turbulence structure in the natural flow case was investigated by comparing data at the flat, 15°, 30°, and 60° stations. The latter three stations were roughly five, ten, and twenty initial boundary-layer thicknesses, δ_0, downstream of the start of the curve. Data in the curve were taken at $z = -5$ cm, the representative location. Profiles at each streamwise station of selected turbulence quantities are presented in figure 17 (*a–l*), with U_{pw} and δ_{99} used for scaling.

As expected, concave curvature causes turbulence intensities to increase significantly across most of the boundary layer. Figures 17 (*a*) and 17 (*b*) show profiles of u'/U_{pw} and v'/U_{pw}, respectively. Increases in u' are moderate and appear to be well established by the first station in the curve. Changes in v' are much greater. The peak value of v' increases by about 50% between the flat and 60° stations, and the location of the peak moves from about $y/\delta = 0.2$ to about $y/\delta = 0.4$. Profiles of the ratio v'/u' are shown in figure 17 (*c*) and give a clear indication that v' is affected more strongly than u'. At each streamwise station, v'/u' is nearly constant between $y/\delta \approx 0.3$ and $y/\delta \approx 0.8$, but the values in this region increase from about 0.65 at the flat station to about 0.88 at 60°. The ratio at 60° translates to a ratio of Reynolds normal stresses of $\langle v^2\rangle/\langle u^2\rangle = 0.77$, which is quite high for a boundary layer.

Figure 17 (*d*) shows that the Reynolds shear stress, $-\langle uv\rangle$, increases dramatically across the middle of the boundary layer. Like the peak in v', the peak in the shear-stress profile moves out to roughly $y/\delta = 0.4$. Profiles at the 30° and 60° stations are quite similar, indicating that the major changes in shear stress have been completed by the 30° station, which is at $x/\delta_0 \approx 10$.

The large increase in $-\langle uv\rangle$ is due in part to the overall increases in u' and v' and in part to a substantial increase in the correlation coefficient, R_{uv}, which is plotted in figure 17 (*e*). R_{uv} remains between 0.4 and 0.45 across most of the flat boundary layer from $y^+ = 10$ to $y/\delta = 0.8$, approximately. Similar values are found close to the wall in the concave boundary layer, but R_{uv} is as high as 0.64 in the middle of the boundary layer at the 60° station. The R_{uv} profiles exhibit small but distinct local

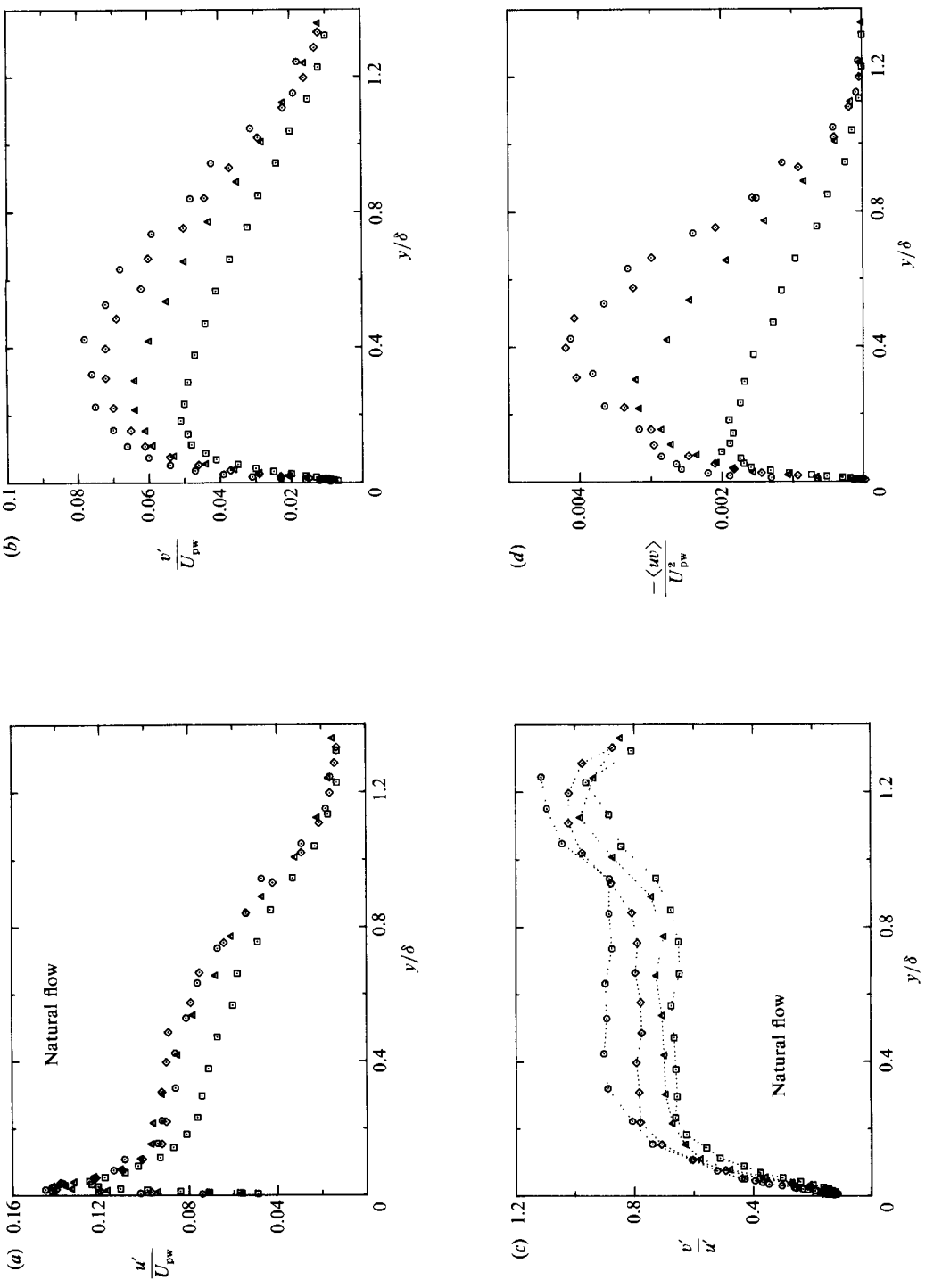
(a)
Natural flow
$\frac{u'}{U_{pw}}$
0.16
0.12
0.08
0.04
0
0.4
0.8
1.2
y/δ
(b)
$\frac{v'}{U_{pw}}$
0.1
0.08
0.06
0.04
0.02
0
0.4
0.8
1.2
y/δ
(c)
Natural flow
$\frac{v'}{u'}$
1.2
0.8
0.4
0
0.4
0.8
1.2
y/δ
(d)
$-\frac{\langle uv \rangle}{U_{pw}^2}$
0.004
0.002
0
0.4
0.8
1.2
y/δ

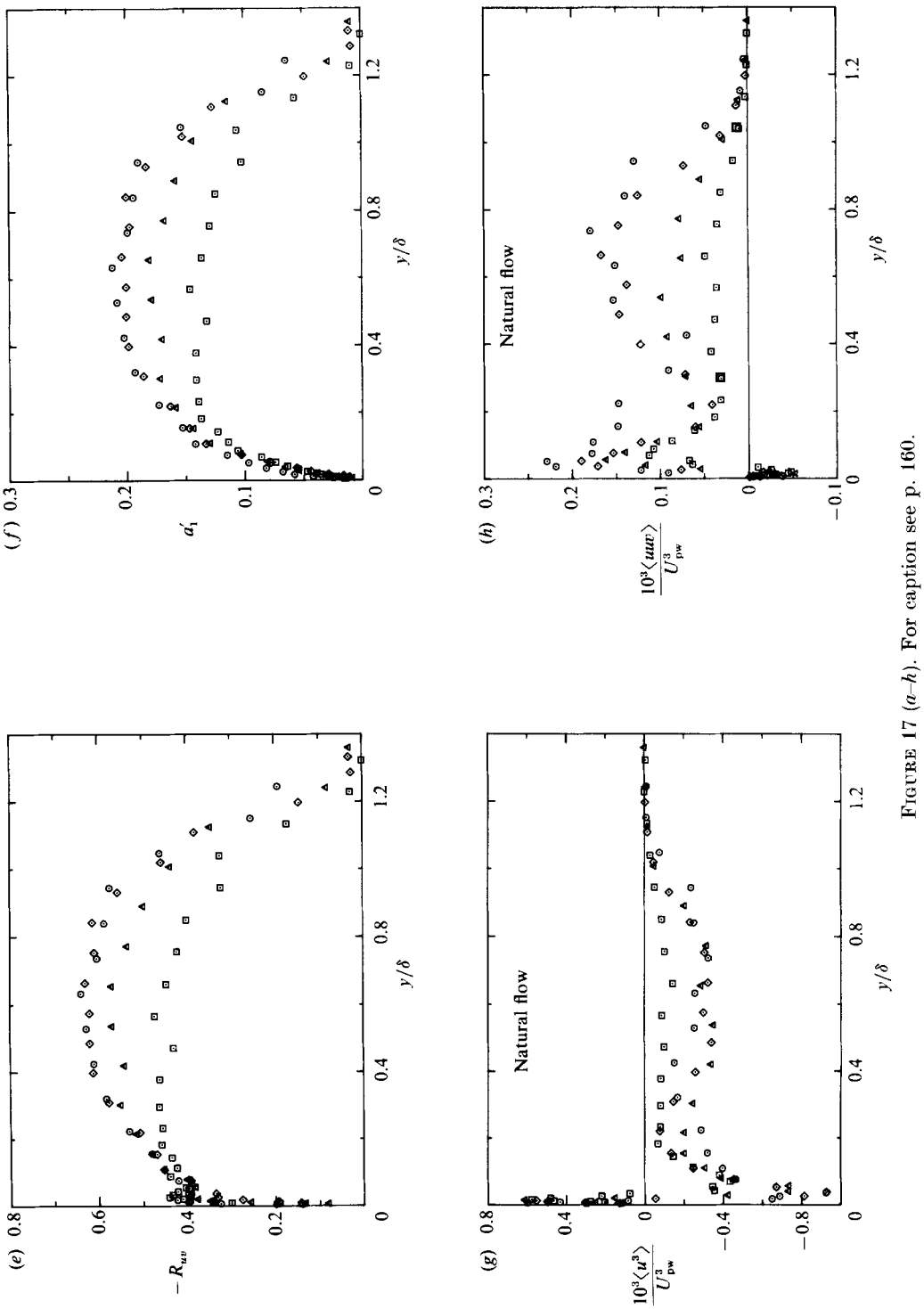

FIGURE 17 (*a–h*). For caption see p. 160.

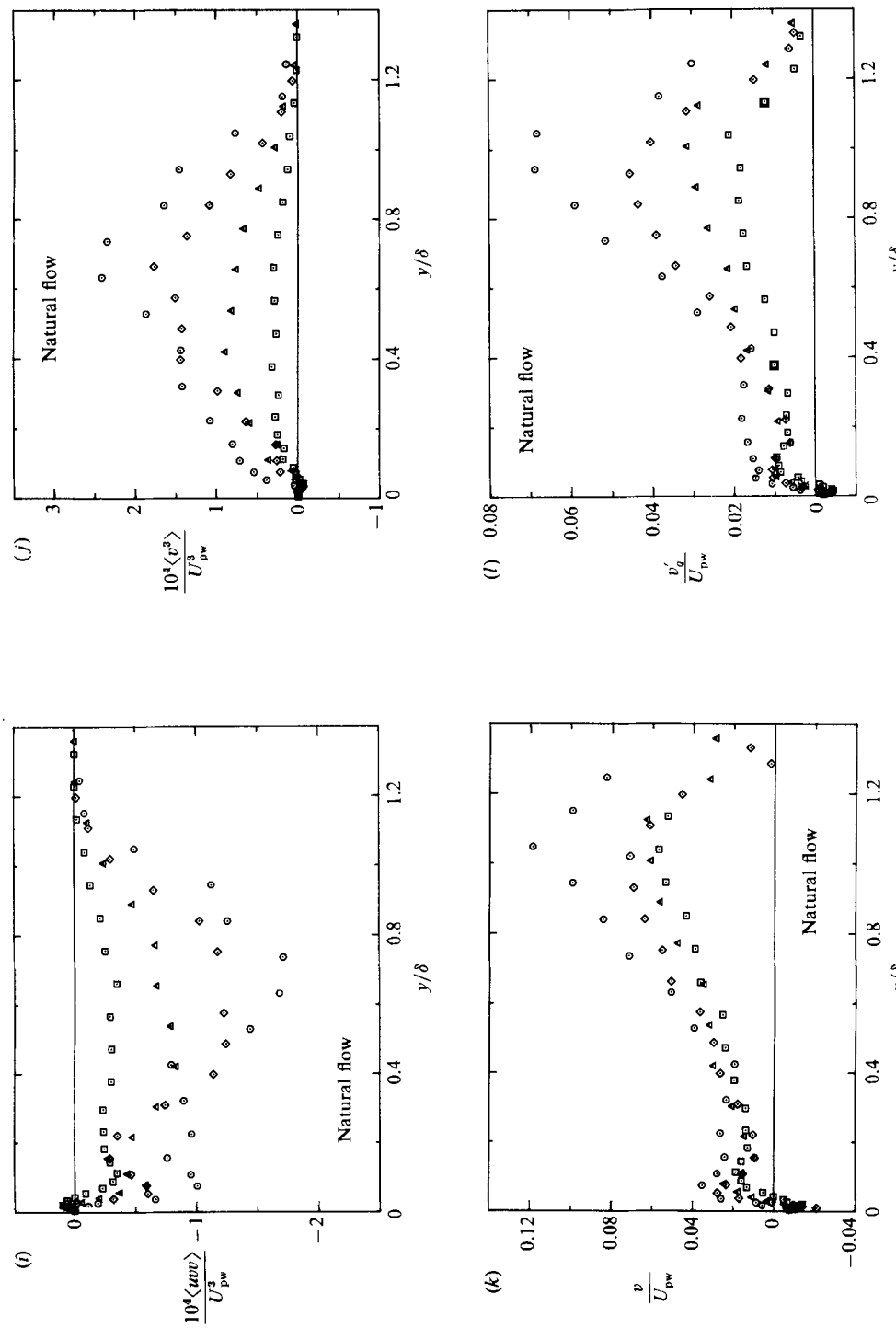

FIGURE 17. (*a, b*) Streamwise development in the natural flow of the profiles of: (*a*) u'/U_{pw}; (*b*) v'/U_{pw}; (*c*) v'/u'; (*d*) $-\langle uv\rangle/U_{pw}^2$; (*e*) $-R_{uv} = -\langle uv\rangle/(\langle u^2\rangle\langle v^2\rangle)^{\frac{1}{2}}$; (*f*) $a'_1 = \langle uv\rangle/1.5(\langle u^2\rangle+\langle v^2\rangle)$; (*g*) $\langle u^3\rangle/U_{pw}^3$; (*h*) $\langle u^3v\rangle/U_{pw}^3$; (*i*) $\langle uv^2\rangle/U_{pw}^3$; (*j*) $\langle v^3\rangle/U_{pw}^3$; (*k*) V_r/U_{pw}, (*l*) V'_q/U_{pw}. □, flat; △, 15°; ◇, 30°; ○, 60°.

peaks close to the wall, in the region of peak streamwise turbulence intensity. Similar local maxima in R_{uv} profiles appear in results of numerical simulations by Moin & Kim (1982) and Moser & Moin (1984, 1985).

The shear-stress parameter, a_1, is defined as $-\langle uv\rangle/q^2$, where $q^2 = \langle u^2\rangle + \langle v^2\rangle + \langle w^2\rangle$. An analogous parameter for two-component data is a_1', which is defined as $-\langle uv\rangle/1.5(\langle u^2\rangle + \langle v^2\rangle)$. The behaviour of a_1', shown in figure 17(*f*), is similar to that of the correlation coefficient. In the middle of the boundary layer, a_1' increases by about 40% between the flat and 30° stations. However, no further increase occurs after 30° ($x/\delta_0 \cong 10$).

The parameters, v'/u', R_{uv}, and a_1', give the clearest picture of the effects of destabilizing curvature on the structure of turbulence in the outer layer. The centrifugal mechanism tends to drive high-momentum fluid toward the wall, while low-momentum fluid is displaced and driven away from the wall. These motions are, of course, negatively correlated, as reflected by the increases in R_{uv} and a_1'. Velocity fluctuations normal to the wall are affected most directly, as shown by the increase in v'/u' relative to the value of this ratio on the flat wall.

The triple products, $\langle u^3\rangle$, $\langle u^2v\rangle$, $\langle uv^2\rangle$, and $\langle v^3\rangle$, appear in the diffusion terms of the balance equations for turbulent kinetic energy and shear stress. Using tensor notation, the triple product $\langle u_i u_j u_k\rangle$ is interpreted physically as the tranport of $u_i u_j$ by u_k. Profiles of these four triple products scaled on U_{pw}^3 are plotted in figure 17(*g–j*). All the triple products are increased by curvature, but since normal fluctuations are augmented more than streamwise fluctuations, $\langle v^3\rangle$ shows the greatest increase, while $\langle u^3\rangle$ shows the least. Increases in $\langle u^2v\rangle$, $\langle uv^2\rangle$, and $\langle v^3\rangle$ are particularly large between $y/\delta \approx 0.5$ and $y/\delta \approx 0.9$, with distinct peaks occurring near $y/\delta = 0.7$.

In considering the effects of curvature on turbulent diffusion, it is useful to define turbulent transport velocities of shear stress and turbulent kinetic energy. Here, because spanwise velocity was not measured, a modified form of the kinetic energy transport velocity is used.

$$V_\tau = \langle uv^2\rangle/\langle uv\rangle,$$

$$V_q' = (\langle u^2v\rangle + \langle v^3\rangle)/(\langle u^2\rangle + \langle v^2\rangle).$$

Profiles of these transport velocities, scaled by U_{pw}, are plotted in figure 17(*k*, *l*). V_τ and V_q' are both increased by concave curvature, but V_q' is affected more strongly, such that the peak magnitude of V_q'/U_{pw} nearly triples between the flat and 60° stations. Hoffmann *et al.* also found that V_q' was affected more strongly than V_τ and that V_q' more than doubled under the influence of mild curvature.

3.4. *The response to sudden onset of concave curvature*

The rate of response of a turbulent boundary layer to a step increase in concave geometric curvature is of interest because previous investigators have reached opposite qualitative conclusions regarding the rate of response. Muck (1982) described the response time of the concave boundary layer as 'long', being an order of magnitude longer than the response time of the convex boundary layer. However, Shizawa & Honami (1983) concluded that the boundary layer responded 'rapidly' to curvature. It is more useful to quantify the streamwise distance, x/R or x/δ_0, required to reach a limiting state. For example, the $-\langle uv\rangle/U_{\mathrm{pw}}^2$ profiles for the convex curvature experiments of Gillis & Johnston (1983) appear to reach a limiting state within five boundary-layer thicknesses of the start of convex curvature.

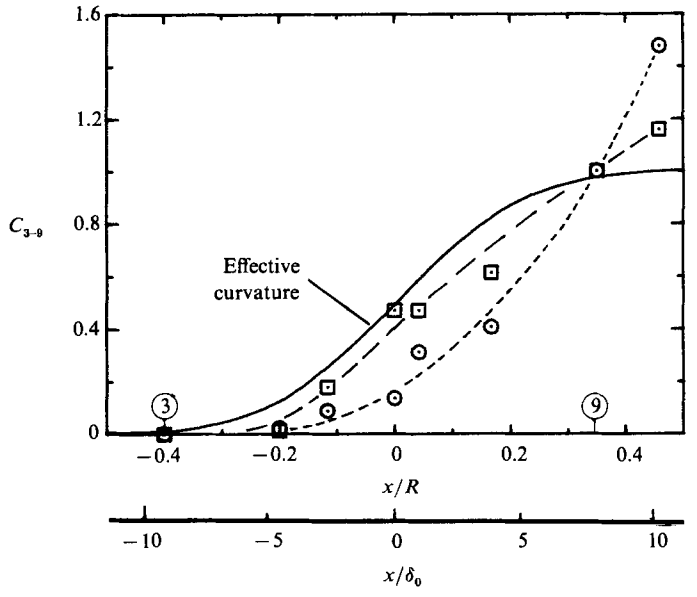

FIGURE 18. Response of □, a_1, and ○, $\frac{1}{2}q^2$ at $y/\delta = 0.5$ to the effective curvature for the data of Shizawa & Honami (1985). The increase in each quantity from its value at the flat station 3 is normalized by the net increase in that quantity between stations 3 and 9, which roughly brackets the region of transition of the effective curvature. $C_{3-9} = [(\ ) - (\ )_3]/[(\ )_9 - (\ )_3]$.

Extended regions of constant-radius curvature are relatively rare in practical applications, particularly for boundary-layer flows. If response of the boundary layer is slow compared to relevant lengthscales in a given application, the accurate prediction of the rate of response by turbulence models will be required.

Although geometric curvature changes as a step function in these experiments, potential flow effects influence a region roughly 1.5 channel widths upstream and downstream of the start of geometric curvature. Consequently, the effective curvature (determined by fitting the velocity profile in the free stream to obtain a curvature parameter analogous to $1/R$, where R is the wall radius (Shizawa & Honami 1983)) felt by the outer layer changes gradually through this region. The data of Shizawa & Honami show that the boundary layer responds to the effective curvature such that changes in turbulence quantities begin upstream of the start of geometric curvature. However, their general conclusion that turbulence quantities respond 'rapidly' to the effective curvature may be somewhat misleading, since the greatest changes in their profiles of $\langle v^2 \rangle$, $\langle uv \rangle$, q^2, and $\langle uv^2 \rangle$ occur downstream of the point at which the effective curvature approaches the geometric curvature. Examination of their data reveals that various turbulence quantities respond at different rates. Values of a_1 and $\frac{1}{2}q^2$ at $y/\delta = 0.5$ are plotted in figure 18 for each streamwise station. The increase in each quantity has been normalized by the difference in that quantity between stations 3 and 9, stations which bracket the region of transition of effective curvature in the experiment of Shizawa & Honami. Significantly, a_1 closely follows the effective curvature (solid curve). In contrast, $\frac{1}{2}q^2$ lags considerably behind the effective curvature and does not begin its steepest increase until after the effective curvature approaches the geometric curvature.

Various turbulence quantities also respond at different rates in the present experiment. Profiles of R_{uv} and a_1' each appear to reach limiting states by the 30°

station, roughly $10\delta_0$ into the curve. However, the mean velocity profiles and profiles of v'/U_{pw}, v'/u', $\langle v^3\rangle/U_{pw}^3$, V_τ, and V_q' are still developing between the 30° and 60° stations. The behaviour of the correlation coefficient and the shear stress parameters suggests that existing eddies in the boundary layer near the start of curvature are affected immediately by radial inertial forces associated with the centrifugal instability mechanism. Higher (than the mean) momentum eddies begin to move toward the wall, while lower momentum eddies move away from the wall. The consequent increase in the magnitude of the uv correlation coefficient occurs within a few boundary-layer thicknesses. Presumably, this happens without a significant increase in the scale of the large eddies. This rapid response of R_{uv} and a_1 to concave curvature is similar to the overall rate of response of a boundary layer to convex curvature, as reported by Gillis & Johnston (1983). However, in contrast to the convex case, which appears to involve simple, rapid attenuation of existing eddies (Muck *et al.* 1985), the further development of the concave boundary layer involves the transfer of energy from the mean flow into the turbulence through the action of the centrifugal mechanism. Visualization results have shown that a new, large-scale eddy structure is created through the amplification of large-scale, negatively correlated motions normal to the wall. This growth of turbulence scales and addition of energy to the larger scales, which result in the observed roll-cell structure, apparently takes considerably longer than the initial redirection of existing eddies. Consequently, q^2 and other turbulence quantities reflecting fluctuations normal to the wall continue to increase after the major changes in R_{uv} and a_1 have been completed.

As stated previously, data on the streamwise development of C_f (figure 15) indicate that, although major structural changes have occurred by the 60° station, roughly $20\delta_0$ from the start of curvature, the boundary layer has not fully responded to the effects of curvature. This is consistent with the C_f data of Hoffmann *et al.* (1985), which show a peak in spanwise average skin friction at roughly $27\delta_0$ followed by a slight decrease. These results suggest that the boundary-layer response distance for adjustment to concave curvature scales with δ_0. Scaling by the wall radius, R, would be clearly inappropriate for these two cases, where δ_0/R differs by a factor of approximately 5. Given the sparseness of data, this δ_0 scaling can be offered only as a tentative conclusion. However, if confirmed, it would be useful for modelling.

3.5. *Near-wall profiles*

It has been argued that curvature should have a smaller effect on the near-wall region than on the outer layer, because the strain-rate ratio $(\bar{U}/r)/(\partial\bar{U}/\partial y)$, diminishes approaching the wall (Bradshaw 1973). The mean velocity profiles in figure 14 are consistent with this view, showing similarity out to roughly $y^+ = 50$. However, flow visualization (figure 7) has suggested that the large-scale inflows and outflows of the concave layer have a much stronger influence on near-wall structure than large eddies in a normal, flat boundary layer. Furthermore, direct numerical simulation of a fully developed, curved, turbulent channel flow by Moser & Moin (1984, 1985) has shown that differences between convex and concave sides extend all the way to the wall for some turbulence quantities.

In this section, near-wall statistics at the 60° station and the flat station, 88 cm upstream of the start of curvature, are compared. (Results presented in the previous sections suggest that major structural changes in the boundary layer have occurred by the 60° station.) Because no previous studies of concave boundary layer have included detailed near-wall measurement, various aspects of the present data are

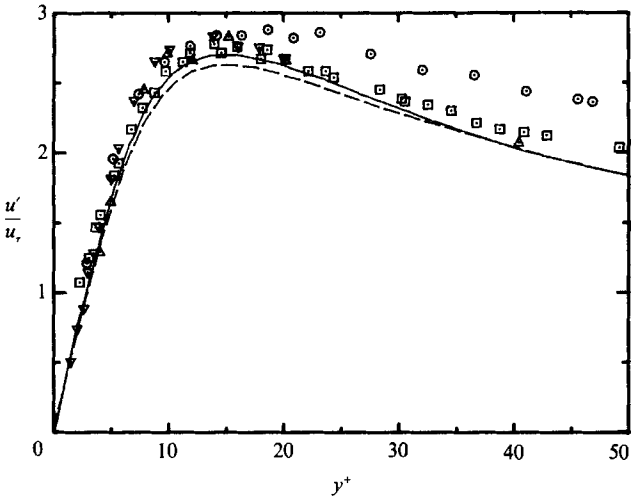

FIGURE 19. Streamwise turbulence intensity, u'/u_τ: □, flat station; ○, 60° station; △, Purtell *et al.* (1981); ▽, Kreplin & Eckelmann (1979); ——, Moser & Moin (1984), concave channel wall; – – –, Moser & Moin, convex channel wall.

compared with flat boundary-layer data of Purtell, Klebanoff & Buckley (1981), Ueda & Hinze (1975), and Schubauer (1954), with the straight-channel data of Eckelmann (1974) and Kreplin & Eckelmann (1979), and with results of the direct numerical simulation of a curved channel flow by Moser & Moin (1984, 1985) and of straight channel flow by Kim, Moin & Moser (1988). All data are plotted on a linear scale out to $y^+ = 50$, the approximate limit of near-wall similarity in the mean velocity profiles. The local u_τ, as determined by the Clauser method ($\kappa = 0.41$, $C = 5.0$), is used for scaling.

Profiles of the normalized streamwise turbulence intensity, u'/u_τ, are shown in figure 19. All the data shown, both experimental and computational, are at relatively low Reynolds numbers, and the present results for the flat boundary layer show good agreement with the literature. From about $y^+ = 15$ outward, the u' turbulence intensity in the concave boundary layer is higher than in the flat case by an amount in excess of the uncertainty. This is in contrast with results from the simulation of a fully developed, curved channel flow, which show only a slight difference between the convex and concave sides near the region of peak turbulence intensity.

Inside $y^+ \approx 15$, the present data show no measurable difference in u'/u_τ between the flat and concave cases. Recall from figure 4 that concave curvature causes only minor changes in the near-wall profile of $u'/\bar{U}$, the turbulence intensity scaled by the local mean velocity. Within y^+ of 5, the turbulence contribution to the total shear stress is very small and the instantaneous velocity profile is nearly linear. Therefore, fluctuations of streamwise velocity are nearly proportional to fluctuations of wall shear, i.e. $u'/\bar{U} \approx \tau'_w/\overline{\tau_w}$. The observed similarity of the $u'/\bar{U}$ profiles and of the u'/u_τ profiles close to the flat and concave walls suggests that the r.m.s. variation of wall shear stress is not affected significantly by curvature. Apparently, the large-scale inflows and outflows do not cause fluctuations in wall shear that are larger, relative to the mean, than the fluctuations of wall shear in a normal flat boundary layer.

Profiles of turbulence intensity normal to the wall, v'/u_τ, are shown in figure 20. (As indicated in §2 and illustrated in figure 6, the present v' data begin to lose accuracy somewhere inside $y^+ \approx 10$, due to diminishing signal-to-noise ratio.) We

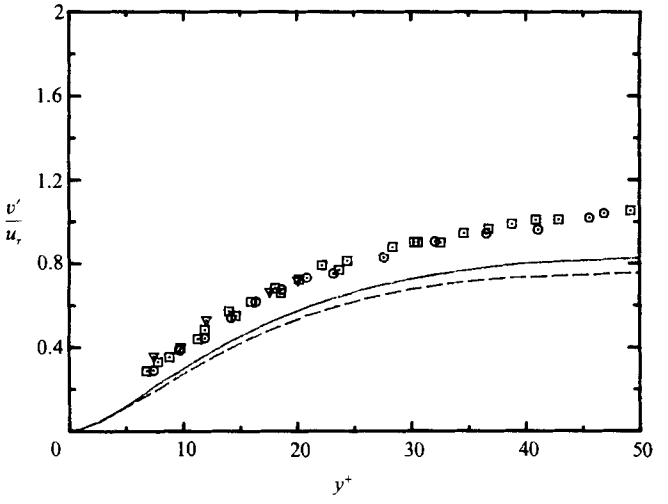

FIGURE 20. Normal turbulence intensity, v'/u_τ; □, flat station; ○, 60° station; ▽, Kreplin & Eckelmann (1979); ——, Moser & Moin (1984), concave channel wall; ——, Moser & Moin, convex channel wall.

find no measurable difference between the flat and concave boundary layers in the present experiment, and there is good agreement between the present results and the data of Kreplin & Eckelmann. However, there is a discrepancy between experimental and numerical results. Kim *et al.* (1988) discuss this discrepancy between experimental and computational results and suggest that a cross-contamination mechanism described by Perry, Lim & Henbest (1985) may contribute to experimental uncertainty in hot-wire measurements. The present LDA technique used a 0°/90° beam orientation with frequency shifting such that the signal for velocity normal to the wall was nominally independent of the streamwise and spanwise velocities. There are sources of error due to the fact that fringes are not perfectly parallel to the wall, but the resulting errors are believed to be small. By necessity, the optical axis of the laser beams comes into the wall at the slight angle of about 2.5°. Thus, a small component of spanwise velocity enters the v-signal. However, since the vw correlation coefficient can be assumed to be nearly zero, the contribution to the v' turbulence intensity is negligible. Similarly, if the plane containing the two beams measuring the normal velocity is not perpendicular to the wall, a component of the streamwise velocity enters the v-signal. However, the LDA system was aligned to null the signal for $\overline{V}$, the mean velocity normal to the wall, at points closest to the wall, so that the v' uncertainty due to this effect is believed to be less than 1%. The greatest uncertainty in the v'/u_τ profiles is due to uncertainty in u_τ, the friction velocity, which is estimated at $\pm 3\%$, in the flat boundary layer. Therefore, to the best of our knowledge, the difference between experimental and numerical results for v'/u_τ is greater than the uncertainty in the present experimental data set. Further investigation of this issue needs to be carried out to determine the cause of this difference.

The Reynolds shear stress and the correlation coefficient are shown in figures 21 and 22, respectively. Data for the flat and concave cases both compare favourably with the flat boundary-layer data of Schubauer. It is only outside $y^+ = 30$ that the trend toward higher Reynolds shear stress in the concave boundary layer begins to appear. At $y/\delta = 0.4$ the shear stress at the 60° station is more than twice that at the

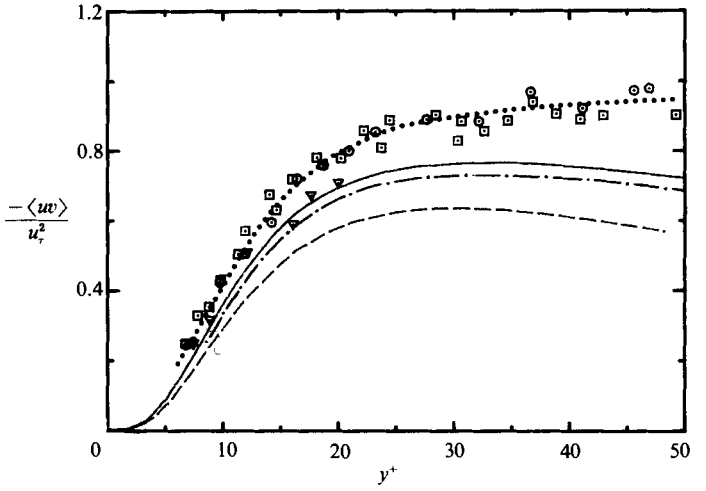

FIGURE 21. Reynolds shear stress, $-\langle uv\rangle/u_\tau^2$: □, flat station; ○, 60° station; ▽, Eckelmann (1974); · · · · ·, Schubauer (1954); ——, Moser & Moin (1984), concave; —·—, Kim *et al.* (1986 straight channel); – – –, Moser & Moin, convex channel wall.

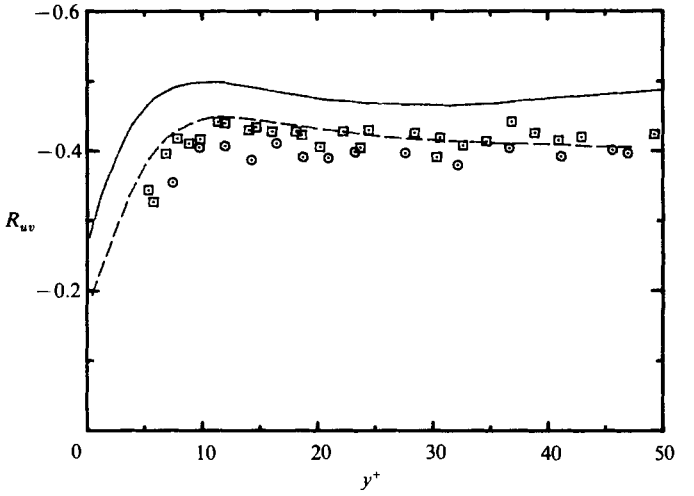

FIGURE 22. Correlation coefficient, R_{uv}: □, flat; ○, 60°; ——, Moser & Moin (1984), concave; – – –, Moser & Moin, convex.

flat station. Total stress is nearly constant in the wall region of a boundary layer but decreases linearly with distance from the wall in a channel flow, so Reynolds stress profiles for boundary-layer and channel flow are expected to be different. Considering the three computed channel-flow cases, convex curvature causes a larger change in $-\langle uv\rangle/u_\tau^2$ than concave curvature. The difference between the computed flat and concave cases is small. A similar difference between flat and concave boundary layers could not be resolved within the scatter in the present data. The data in figure 22 confirm the local maximum in the correlation coefficient, R_{uv}, in the region of peak turbulence production near $y^+ = 12$.

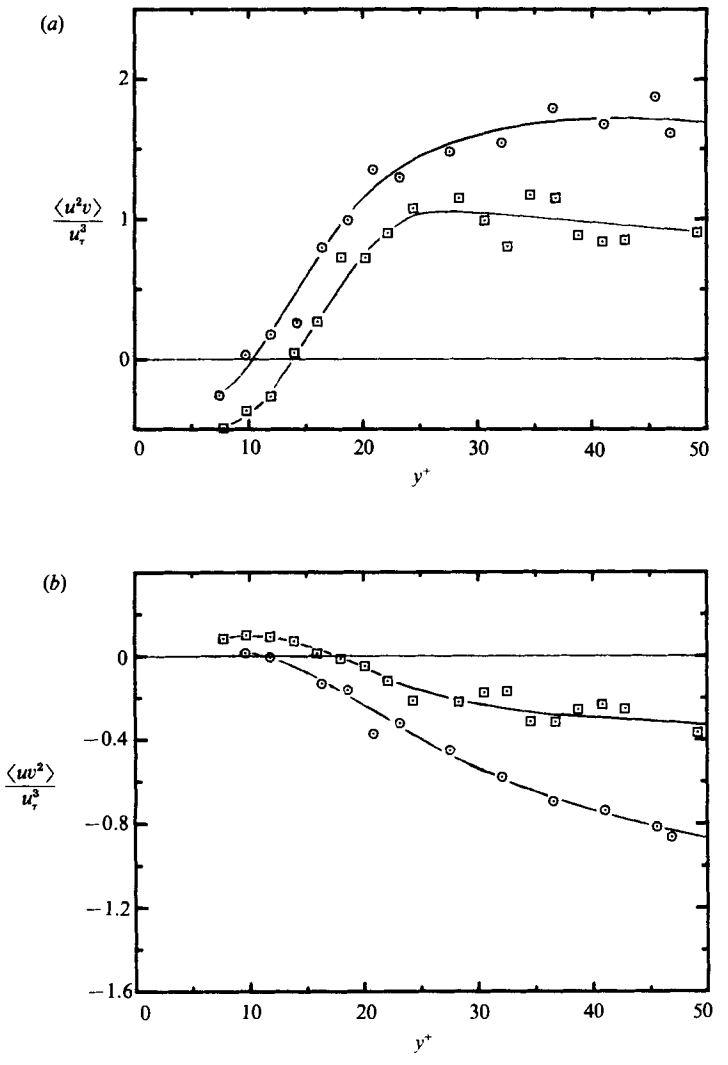

FIGURE 23. Triple products, (*a*) $\langle u^2v\rangle/u_\tau^3$; (*b*) $\langle uv^2\rangle/u_\tau^3$: □, flat; ○, 60°.

Figures 23(*a*) and 23(*b*) show profiles of the triple products $\langle u^2v\rangle$ and $\langle uv^2\rangle$, respectively. These products appear in the diffusion terms of the balance equations for turbulent kinetic energy and shear stress. Here we find distinct differences between the flat and concave boundary layers. Profiles in the curve change sign near $y^+ = 10$, rather than near $y^+ = 15$, and the magnitudes of these triple products through the range $20 \leqslant y^+ \leqslant 50$ are significantly higher in the concave boundary layer.

Profiles of the turbulent transport velocities, V_τ and V'_q, are shown in figure 24(*a*, *b*). Concave curvature has a greater effect on V_τ than on V'_q in the near-wall region. Recall from figure 18(*k*, *l*) that V'_q was more strongly affected across the outer layer.

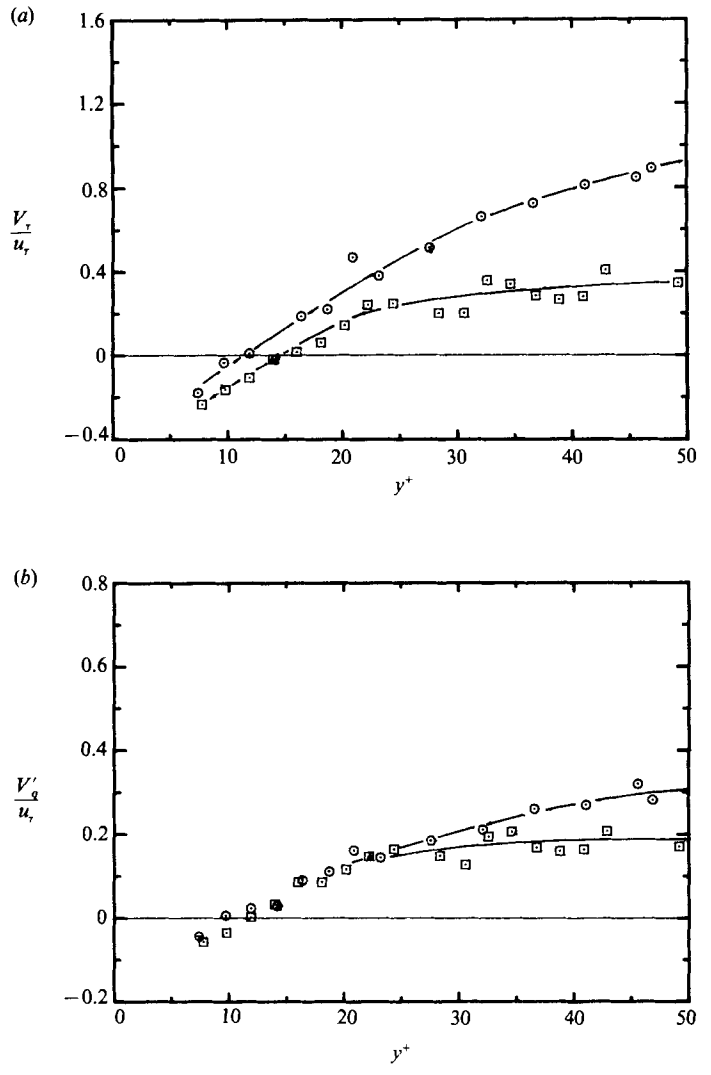

FIGURE 24. Turbulent transport velocities, (a) V_τ/u_τ; (b) V'_q/u_τ: □, flat; ○, 60°.

Skewness and flatness factors are plotted in figures 25 and 26. There is generally good agreement between the present data and the literature on the statistics of streamwise velocity fluctuations. As for the triple products, the zero crossing of u-skewness is closer to the wall in the concave flow. The location of the minimum in the u-flatness profile behaves similarly. Measurements of the skewness and flatness of v fluctuations are clearly less accurate near the wall. Nevertheless, the present data confirm the negative v-skewness in the region of peak turbulence production, a feature not present in the data of Kreplin & Eckelmann. The full simulations predict very high v-flatness in the wall region. Outside y^+ of about 8, the accuracy limit of the present v data, agreement between measured and computed profiles is good. At a given distance from the wall, one finds that v-flatness is higher in the concave cases than in the flat cases. This relationship, combined with the fact that the v-skewness

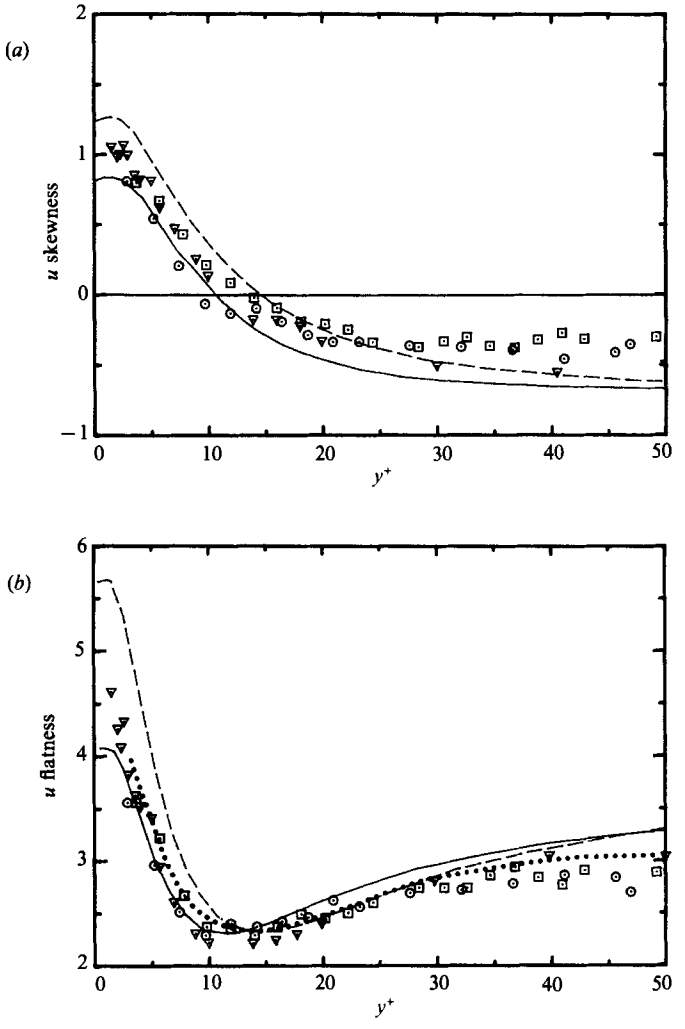

FIGURE 25. (*a*) Skewness and (*b*) flatness of u: □, flat station; ○, 60° station; ▽, Kreplin & Eckelmann (1979); ——, Moser & Moin (1984), concave; ——, Moser & Moin, convex; · · · · ·, Ueda & Hinze (1975).

profiles for the concave flows lie above those for the flat flows, indicates that strong motions away from the wall are more common in the concave boundary layer. This interpretation is consistent with flow visualization, which shows that the large-scale inflows impinge on the wall over broad regions (in the spanwise sense), while sublayer fluid tends to leave the wall in relatively narrow regions. (Mean-velocity and skin-friction data in Barlow & Johnston (1988) for the flow with vortex generators also show that inflows are wider than outflows.)

In summary, the present data for the natural flow show that, while concave curvature produces a significant increase in wall shear, near-wall profiles of mean velocity and the measured Reynolds stresses scaled on the local u_τ in the concave boundary layer are generally the same as near-wall profiles in the flat boundary layer. Similarly holds through the sublayer and across the region of peak turbulence

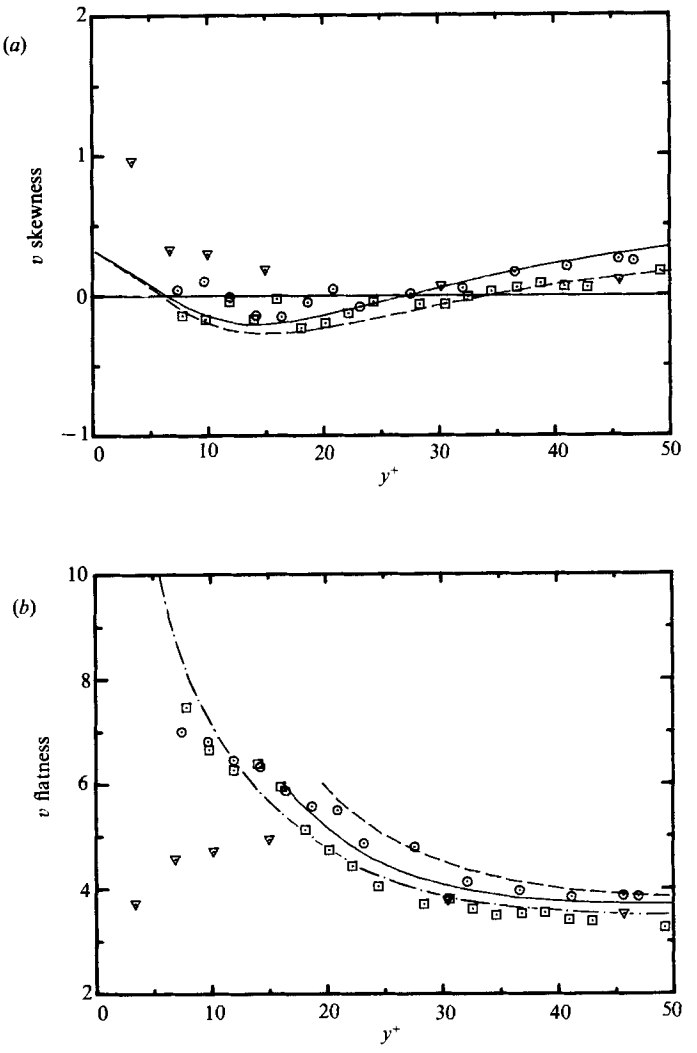

FIGURE 26. (*a*) Skewness and (*b*) flatness of v: □, flat station; ○, 60° station; ▽, Kreplin & Eckelmann (1979); ——, Moser & Moin (1984), concave; —·—, Kim *et al.* (1986), straight channel; – – –, Moser & Moin, convex.

production. This implies that the production process is not significantly altered by concave curvature, at least in the statistical sense, in spite of the dramatic differences in visualized, near-wall structure. Profiles of triple products show clear differences between the two cases, indicating that curvature has a greater effect on diffusion than on production. However, the influence of the intermittent, large-scale inflows and outflows on near-wall, Reynolds-averaged statistics are minor compared to their visual effects on the wall region.

3.6. *Spectra*

One might expect the presence of the large-scale roll cells to be reflected in the energy spectra as an increase in the energy content at low frequencies. Hunt & Joubert (1979) measured the energy spectra of streamwise, u, velocity fluctuations in straight

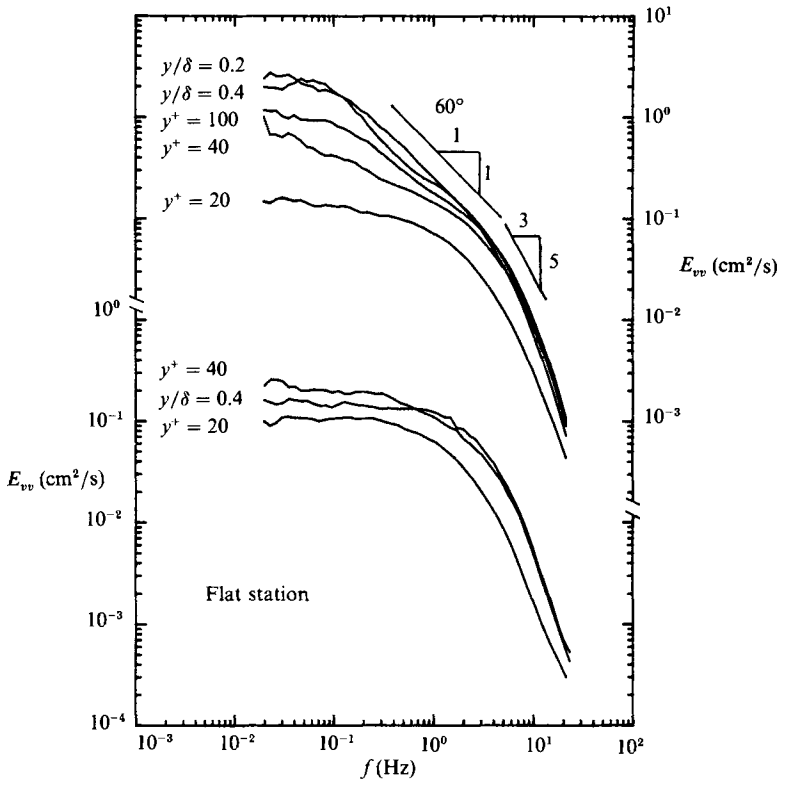

FIGURE 27. Comparison of v spectra in the flat and 60° boundary layers.

and mildly curved duct flows. They found that differences among the flat, concave, and convex cases were confined to the low-frequency range, and they concluded that differences in u', the streamwise turbulence intensity, could be attributed to changes in the energy content of the low-frequency, large-scale fluctuations alone. In the present study, spectra of the u, v, and uv fluctuations are considered, with particular attention given to the energy-containing frequencies.

The effects of concave curvature on the v spectra are examined in figure 27, which includes results at several y-locations in the flat and 60° boundary layers. Near the wall, at $y^+ = 20$, v spectra are similar in the flat and concave boundary layers. In the flat boundary layer, there is little change in the shape of the v spectrum with distance from the wall. However, in the concave boundary layer the distribution of energy changes significantly with distance from the wall. At high frequencies, the energy content of the turbulence is about the same as in the flat boundary layer for all y-locations, suggesting that the small-scale turbulence structure is essentially unaffected by curvature. In contrast, the energy content in the low-frequency range increases dramatically with distance from the wall. This increase is already apparent at $y^+ = 40$, but it is most significant in the middle of the boundary layer. At $y/\delta = 0.2$ and 0.4, there are extended regions of approximately -1 slope that are not present in the spectra in the flat boundary layer. These comparisons of v spectra show that the increase in v' can be attributed almost entirely to increased energy in the low-frequency, large-scale turbulent fluctuations.

The -1 region of the u spectrum in a flat boundary layer reflects the direct

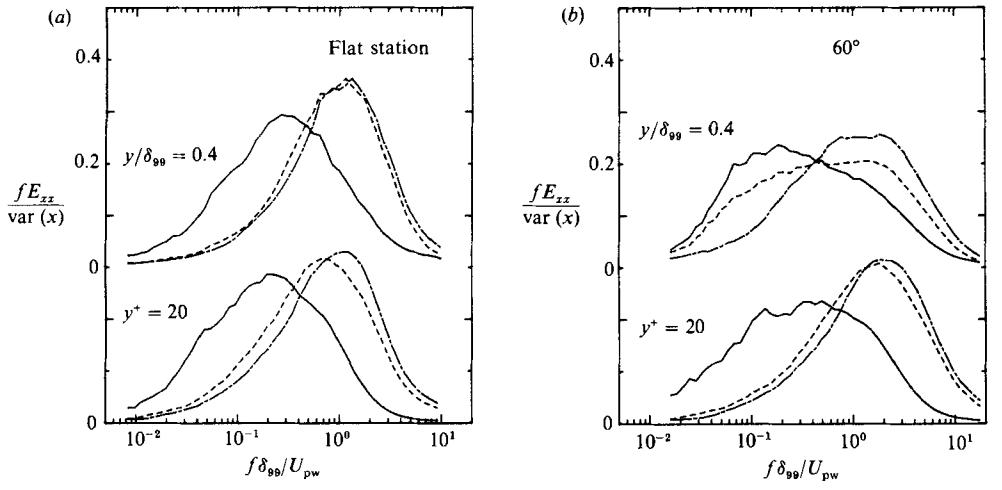

FIGURE 28. Comparison of ——, u; – – –, v; —·—, uv spectra at $y^+ = 20$ and $y/\delta = 0.4$ in the (*a*) flat and (*b*) 60° boundary layers.

coupling (energy transfer) between the mean flow and the streamwise turbulent fluctuations (Perry *et al.* 1985). Similarly, the extended -1 regions in the v spectra at $y/\delta = 0.2$ and $y/\delta = 0.4$ in the concave layer (figure 27) are believed to reflect a direct energy transfer from the mean flow to v fluctuations through the centrifugal mechanism.

The effects of destabilizing curvature on the energy-containing ranges of u, v, and uv fluctuations are examined in figure 28. Here, the product of frequency and energy content normalized by the variance is plotted to facilitate visual interpretation of the energy-containing range of each spectrum. (The total energy in, say, streamwise fluctuations is proportional to $\langle u^2 \rangle = \int E_u(f)\,\mathrm{d}f = \int fE_u(f)\,\mathrm{d}(\ln(f))$. Therefore, visual integration of the curves in figure 28 can be used to identify the energy-containing ranges. The peak of each curve corresponds to the portion of the raw spectrum having a -1 slope. The region around the peak accounts for most of the area under each curve – hence most of the energy.) Spectra are included for two y-locations in the flat and 60° boundary layers. $y^+ = 20$ is representative of the near-wall region, and $y/\delta = 0.4$ is representative of the middle of the boundary layer, where the roll cells appear to have greatest influence.

Results are similar at the two locations in the flat boundary layer and at $y^+ = 20$ in the concave boundary layer. Peaks in the v spectra occur at higher frequencies than in the u spectra by factors of four to five. The peaks of the v spectra are also somewhat narrower than those of the u spectra. This separation of u and v spectra causes the frequency content of the uv signal to be dominated by v fluctuations, such that the uv spectra are quite close to the v spectra in these three cases.

Results at $y/\delta = 0.4$ in the concave boundary layer are very different. Here, the energy-containing ranges of the u, v, and uv spectra have all broadened and shifted toward lower frequencies, reflecting increased turbulent energy in larger-scale fluctuations. This is particularly pronounced in the v spectrum, which has broadened to include a substantial part of the energy-containing range of the u spectrum. The separation of u and v signals in frequency no longer exists, causing the similarity between v and uv spectra to disappear.

4. Conclusions

Detailed measurements have been made in a concave boundary layer where the behaviour of the large-scale structures produced by destabilizing curvature was thoroughly documented through flow visualization. When the boundary layer approaching the curve is relatively free of spanwise non-uniformities, the large-scale structures (inflows and outflows) wander, merge, separate, appear, and disappear. They do not produce significant spanwise variations in the mean properties of the boundary layer. These large-scale structures occupy ranges of length and energy scales. They are larger than typical large eddies in a flat boundary layer and are more energetic, particularly with regard to fluctuations normal to the wall. However, they need not be considered as fundamentally different, and it would be inappropriate to describe these structures, which are typically only 3δ to 5δ in length, as longitudinal vortices.

Generally, the measurements reported here are consistent with previous studies and with the expected influence of destabilizing curvature. They show that the primary effect of concave curvature is to amplify large-scale, negatively correlated eddies. Fluctuations normal to the wall are affected most, due to a direct coupling between the mean flow and the v' turbulence that does not exist in a flat boundary layer. Mixing across the boundary layer is enhanced, bringing high-momentum fluid closer to the wall than in a flat boundary layer and causing a significant increase in skin friction.

Increases in turbulence intensities and the Reynolds shear stress across the outer layer are due almost entirely to increased energy in low-frequency, large-scale fluctuations. Very large increases in triple products can also be associated with the more energetic large-scale eddy structure.

The response of the boundary layer to the sudden onset of concave curvature appears to involve two overlapping stages. First, large eddies near the start of curvature are affected immediately by the centrifugal mechanism. Higher (than the mean) momentum eddies begin to move toward the wall, while lower momentum eddies tend to move away from the wall. The resulting increase in the correlation coefficient occurs within a few boundary-layer thicknesses. Presumably, this happens without significant increases in turbulent lengthscales. The further development of the boundary layer requires the slower growth and amplification of the large-scale inflows and outflows, a process that continues for at least $20\delta_0$.

The large-scale inflows and outflows have a much stronger visual effect on the near-wall flow than large eddies in a flat boundary layer. However, in terms of Reynolds-averaged statistics, the near-wall structure is not significantly different from that in a normal flat boundary layer, so long as local u_τ scaling is used. In particular, τ'_w/τ_w, the normalized r.m.s. wall shear, is essentially the same in the concave and flat cases, despite the strong influence of the large-scale roll cells on the visualized near-wall structure.

One implication of these observations for modelling is that, for many applications, two-dimensional models should be adequate, so long as they accurately predict the spanwise average structure. Even in applications in which some upstream non-uniformities are expected, actual spanwise variations from predicted averages are likely to be bracketed by variations measured in flows with vortex generators. Spanwise variations near the wall are less than those across the outer layer, for reasons discussed in Barlow & Johnston (1988), so that engineering calculations of skin friction or heat transfer should not suffer greatly from the assumption of two-

dimensionality. However, accurate prediction of concave flows by turbulence models will require that the slow development of the new large-scale-eddy structure be accounted for.

This work was supported by the Air Force Office of Scientific Research. The authors are grateful to S. J. Kline and R. J. Moffat for many useful discussions during this investigation.

REFERENCES

ADAMS, E. W. & JOHNSTON, J. P. 1983 A mixing length model for the prediction of convex curvature effects on turbulent boundary layers. *ASME Paper* 83-GT-80.

BARLOW, R. S. & JOHNSTON, J. P. 1985 Structure of turbulent boundary layers on a concave surface. *Rept. MD* 47. Thermosciences Div., Dept. of Mech. Engng, Stanford University.

BARLOW, R. S. & JOHNSTON, J. P. 1988 Local effects of large-scale eddies on bursting in a concave boundary layer. *J. Fluid Mech.* **191**, 177.

BLACKWELDER, R. F. & ECKELMANN, H. 1979 On the wall structure of the turbulent boundary layer. *J. Fluid Mech.* **76**, 577.

BLACKWELDER, R. F. & HARITONIDIS, J. H. 1983 Scaling of burst frequencies in turbulent boundary layers. *J. Fluid Mech.* **132**, 87.

BRADSHAW, P. 1965 The effect of wind-tunnel screens on nominally two-dimensional boundary layers. *J. Fluid Mech.* **22**, 679.

BRADSHAW, P. 1973 Effects of streamline curvature on turbulent flow. *AGARDograph* 169.

BROWN, A. & MARTIN, B. W. 1982 Flow transition phenomena and heat transfer over the pressure surfaces of gas-turbine blades. *ASME J. Engng for Power*, **104**, 360.

BROWN, G. L. & THOMAS, A. S. W. 1977 Large structure in a turbulent boundary layer. *Phys. Fluids* **20**, S243.

CRANE, R. I. & SABZVARI, J. 1984 Laser-Doppler measurements of Görtler vortices in laminar and low-Reynolds-number turbulent boundary layers. In *Laser Anemometry in Fluid Mechanics* (ed. R. J. Adrian). Lisbon: Ladoan.

ECKELMANN, H. 1974 The structure of the viscous sublayer and adjacent wall region in a turbulent channel flow. *J. Fluid Mech.* **65**, 439.

ESKINAZI, S. & YEH, H. 1956 An investigation on fully developed turbulent flows in a curved channel. *J. Aero. Sci*, **23**, 23.

FALCO, R. E. 1977 Coherent motions in the outer region of turbulent boundary layers. *Phys. Fluids* **20**, S124.

FALCO, R. E. 1978 The role of outer-flow coherent motions in the production of turbulence near a wall. In *Coherent Structure of Turbulent Boundary Layers*, AFOSR/Lehigh Workshop, Nov. 1978.

GIBSON, M. M., JONES, W. P. & YOUNIS, B. A. 1981 Calculation of turbulent boundary layers on curved surfaces. *Phys. Fluids* **24**, 386.

GILLIS, J. C. & JOHNSTON, J. P. 1983 Turbulent boundary-layer flow and structure on a convex wall and its redevelopment on a flat wall. *J. Fluid Mech.* **135**, 123.

GÖRTLER, H. 1940 Über eine Dreidimensionale Instabilität Laminarer Grenzschichten an Koncaven Wanden. *Ing. Arch.* **28**, 71.

GUPTA, A. K., LAUFER, J. & KAPLAN, R. E. 1971 Spatial structure in a viscous sublayer. *J. Fluid Mech.* **50**, 493.

HOFFMANN, P. H. & BRADSHAW, P. 1981 Turbulent boundary layers on concave surfaces. *Final Report to Brown Boveri Research Centre, Imperial College Aero TN* 81–111.

HOFFMANN, P. H., MUCK, K. C. & BRADSHAW, P. 1985 The effect of concave curvature on turbulent boundary layers. *J. Fluid Mech.* **161**, 371.

HONAMI, S. & JOHNSTON, J. P. 1980 'A new definition of integral thicknesses for boundary-layer flow over longitudinally curved surfaces. *Thermosciences Div. Rep.* IL-26, Dept. of Mech. Engng, Stanford University.

HUMPHREY, J. A. C. & POURAHMADI, F. 1981 A generalized algebraic relation for predicting developing curved channel flow with $k-\epsilon$ model of turbulence. *Third Symp. on Turbulent Shear Flow*, Davis, CA.

HUNT, I. A. & JOUBERT, P. N. 1979 Effects of small streamline curvature on turbulent duct flow. *J. Fluid Mech.* **91**, 633.

JEANS, A. H. & JOHNSTON, J. P. 1982 The effects of concave curvature on turbulent boundary-layer structure. *Thermosciences Div. Rep.* MD-40, Dept of Mech. Engng, Stanford University.

JEANS, A. H. & JOHNSTON, J. P. 1983 The effects of concave curvature on turbulent boundary-layer structure. IUTAM Symposium on *Structure of Complex Turbulent Shear Flow* (ed. R. Dumas & L. Fulachier), p. 89. Springer.

KARPUK, M. E. & TIEDERMAN, W. G. 1976 Effect of finite-size probe volume upon laser-Doppler anemometry measurements. *AIAA J.* **14**, 1099.

KIM, J., MOIN, P. & MOSER, R. 1987 Turbulence statistics in fully developed channel flow at low Reynolds number. *J. Fluid Mech.* **177**, 133.

KLINE, S. J. & RUNSTADLER, P. W. 1959 Some preliminary results of visual studies of the wall layers of the turbulent boundary layer. *Trans ASME* E: *J. Appl. Mech.* **81**, 166.

KOVASZNAY, L. S. G., KIBENS, V. & BLACKWELDER, R. F. 1970 Large-scale motion in the intermittent region of a turbulent boundary layer. *J. Fluid Mech.* **41**, 283.

KREPLIN, H.-P. & ECKELMANN, H. 1979 Behavior of the three fluctuating velocity components in the wall region of a turbulent channel flow. *Phys. Fluids* **22**, 1233.

LEZIUS, D. K. & JOHNSTON, J. P. 1976 Roll-cell instabilities in rotating laminar and turbulent channel flows. *J. Fluid Mech.* **77**, 153.

MERONEY, R. N. & BRADSHAW, P. 1975 Turbulent boundary-layer growth over a longitudinally curved surface. *AIAA J.* **13**, 1448.

MOIN, P. & KIM, J. 1982 Numerical investigation of turbulent channel flow. *J. Fluid Mech.* **118**, 341.

MOSER, R. & MOIN, P. 1984 Direct numerical simulation of curved turbulent channel flow. *Thermosciences Div. Rep.* TF-20, Dept. of Mech. Engng, Stanford University.

MOSER, R. D. & MOIN, P. 1985 Effects of wall curvature on turbulence statistics. Presented at the Fifth Symposium on Turbulent Shear Flows, Cornell University, Ithaca, NY.

MUCK, K. C. 1982 Turbulent boundary layers on mildly curved surfaces. PhD thesis, Imperial College, London.

MUCK, K. C., HOFFMANN, P. H. & BRADSHAW, P. 1985 The effect of convex curvature on turbulent boundary layers. *J. Fluid Mech.* **161**, 347.

PERRY, A. E., LIM, K. L. & HENBEST, S. M. 1985 A spectral analysis of smooth, flat-plate boundary layers. *Proc. Fifth Symp. on Turbulent Shear Flows, August 7–9, 1985.* Cornell University, Ithaca, NY.

PRABHU, A. & RAO, B. N. S. 1981 Turbulent boundary layers in a longitudinally curved stream. *Dept of Aero. Engng Rep.* 81-FM-10. India Inst. Sci. Bangalore.

PRABHU, A. & RAO, B. N. S. 1982 Structure and mean-flow similarity in curved turbulent boundary layers. In *Structure of Complex Turbulent Shear Flow* (ed. R. Dumas & L. Fulachier), IUTAM Symposium, Marseille. Springer.

PURTELL, L. P., KLEBANOFF, P. S. & BUCKLEY, F. T. 1981 Turbulent boundary layer at low Reynolds number. *Phys. Fluids* **24**, 804.

RAGAB, S. 1979 Interacting inviscid and laminar viscous flows and some aspects of their stability. PhD dissertation, Virginia Polytechnic Institute and State University, University Microfilms no. 8020226.

RAMAPRIAN, B. R. & SHIVAPRASAD, B. G. 1978 The structure of turbulent boundary layers along mildly curved surfaces. *J. Fluid Mech.* **85**, 273.

RAYLEIGH, O. M. 1917 On the dynamics of revolving fluids. *Proc. R. Soc. Lond.* A **93**, 148.

SCHUBAUER, G. B. 1954 Turbulent processes as observed in boundary layer and pipe. *J. Appl. Phys.* **25**, 188.

SHIZAWA, T. & HONAMI, S. 1983 Experiment on turbulent boundary layers over a concave surface: effects of introduction of curvature. *4th Symp. Turbulent Shear Flows, Karlsruhe, Sept., 1983.*

SHIZAWA, T. & HONAMI, S. 1985 Experiments on turbulent boundary layers over a concave surface – response of turbulence to curvature. Presented at the 5th Symposium on Turbulent Shear Flows, Cornell University, Ithaca, NY.

SIMON, T. W., MOFFAT, R. J., JOHNSTON, J. P. & KAYS, W. M. 1980 Turbulent boundary layer heat-transfer experiments: convex curvature effects, including introduction and recovery. *Thermosciences Div. Rep.* HMT-32, Dept of Mech. Engng, Stanford University.

SIMONICH, J. C. & MOFFAT, R. J. 1982 Local measurements of turbulent boundary-layer heat transfer on a concave surface using liquid crystals. *Rep. HMT*-35, Thermosciences Div., Dept of Mech. Engng, Stanford University.

SMITH, C. R. 1984 A synthesized model of the near-wall behavior in turbulent boundary layers. *Proc. Eighth Symposium on Turbulence* (ed. G. K. Patterson & J. L. Zakin), Dept. of Chem. Engng, University of Missouri–Rolla.

SMITS, A. J., MATHESON, N. & JOUBERT, P. N. 1983 Low-Reynolds-number turbulent boundary layers in zero and favorable pressure gradients. *J. Ship Res.* **27**, 147.

SO, R. M. C. & MELLOR, G. L. 1972 An experimental investigation of turbulent boundary layers along curved surfaces. *NASA* CR-1940.

SO, R. M. C. & MELLOR, G. L. 1975 Experiment on turbulent boundary layers on a concave wall. *Aero. Q.*, **26**, 25.

SO, R. M. C. & MELLOR, G. L. 1978 Turbulent boundary layers with large streamline curvature effects. *J. Appl. Maths Phys.* **29**, 54.

SWEARINGEN, J. D. & BLACKWELDER, R. F. 1983 Parameters controlling the spacing of streamwise vortices on concave walls. *AIAA*-83-0380.

TANI, I. 1962 Production of longitudinal vortices in the boundary layer along a concave wall. *J. Geophys. Res.* **67**, 3075.

UEDA, H. & HINZE, J. O. 1975 Fine-structure turbulence in the wall region of a turbulent boundary layer. *J. Fluid Mech.* **67**, 125–143.

WILLMARTH, W. W. & SHARMA, L. K. 1984 Study of turbulent structure with hot wires smaller than the viscous length scales. *J. Fluid Mech.* **142**, 121–149.